

Chiral numerical renormalization group

Matan Lotem,^{*} Eran Sela,[†] and Moshe Goldstein[‡]

Raymond and Beverly Sackler School of Physics and Astronomy, Tel Aviv University, Tel Aviv 6997801, Israel

The interplay between the Kondo screening of quantum impurities (by the electronic channels to which they couple) and the interimpurity RKKY interactions (mediated by the same channels) has been extensively studied. However, the effect of unidirectional channels (e.g., chiral or helical edge modes of 2D topological materials) which greatly restrict the mediated interimpurity interactions, has only more recently come under scrutiny, and it can drastically alter the physics. Here we take Wilson’s numerical renormalization group (NRG), the most established numerical method for treating quantum impurity models, and extend it to systems consisting of two impurities coupled at different locations to unidirectional channel(s). This is challenging due to the incompatibility of unidirectionality with one of the main ingredients in NRG—the mapping of the channel(s) to a Wilson chain—a tight-binding chain with the impurity at one end and hopping amplitudes which decay exponentially with the distance. We bridge this gap by introducing a “Wilson ladder” consisting of two coupled Wilson chains, and demonstrate that this construction successfully captures the unidirectionality of the channel(s), as well as the distance between the two impurities. We use this mapping in order to study two Kondo impurities coupled to a single chiral channel, showing that all local properties and thermodynamic quantities are indifferent to the interimpurity distance, and correspond to two separate single-impurity models. Extensions to more impurities and/or helical channels are possible.

I. INTRODUCTION

Two-dimensional topological materials exhibit the remarkable property of edge modes in which electrons of a given species can propagate only in one direction [1, 2]. Thus, intrachannel backscattering is forbidden, resulting in channels which remain ballistic over large distances. Coupling such channels, or baths, to quantum impurities, i.e., impurities with an internal degree of freedom (for example, a localized spin), taps onto the exotic world of Kondo physics [3, 4], in which the bath electrons form a coherent manybody screening cloud around the impurity. When considering single-impurity physics, the unidirectionality of the channel(s) does not have significant consequences. This is illustrated in Fig. 1(a): Generally one can choose a basis of the bidirectional channel modes such that the impurity is coupled to the end of the channel, and then “unfold” the channel by interpreting the outgoing (backscattered) modes of the bidirectional channel as the forward-scattered modes of a unidirectional channel. Indeed, a variety of methods for solving quantum impurity problems explicitly rely on this mapping [5–9]. However, clearly such a mapping cannot be generalized to multiple impurities, where the uni- or bidirectionality of the channel(s) becomes important. The interplay between impurities coupled to bidirectional channels typically gives rise to effective RKKY [10–12] interactions, $K\vec{S}_m \cdot \vec{S}_{m'}$, between impurity spins. This results in the transition of the Kondo lattice from a Kondo-screened (heavy-fermion) phase to a magnetically ordered phase

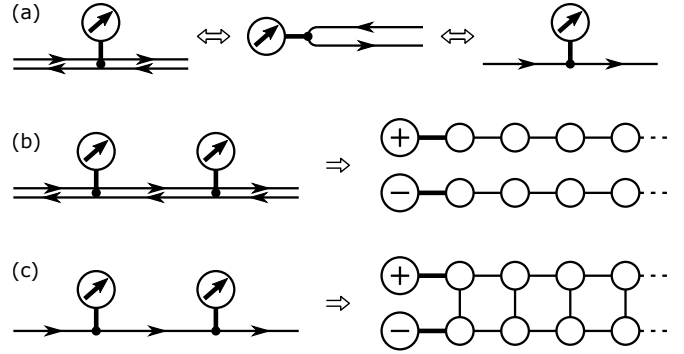


FIG. 1. (a) For a single impurity the coupling to a bidirectional channel can be mapped to a unidirectional channel. (b) For two impurities coupled to a bidirectional channel, after going to an even-odd basis each impurity couples to a separate channel which can be mapped onto a tight-binding (Wilson) chain. (c) However, for two impurities coupled to a unidirectional channel, this mapping is not possible, and instead, we map the channel onto two coupled Wilson chains, or a Wilson ladder.

[13], and has been extensively studied by considering two-impurity models [14–22]. However, if the impurities are coupled to unidirectional channels, the picture is more complicated.

Assuming spinful channels, we have two natural scenarios. The first is *helical* channels, meaning that the two spin species propagate in opposite directions, as in the quantum spin Hall effect [23, 24], so that electrons can only backscatter into the opposite spin channel, flipping the impurity spin in the process. As a result, the z component of the RKKY interaction is forbidden, but the transverse components are still allowed [25]. Taking into account Rashba couplings, intrachannel interactions, and bulk effects further complicates the resulting RKKY

^{*} matanlotem@mail.tau.ac.il

[†] eransx@googlemail.com

[‡] mgoldstein@taux.tau.ac.il

structure and its interplay with the Kondo physics [26–28]. This leads to dramatic consequences on transport properties, and is suspected to be responsible for the breaking of quantized conductance in quantum spin Hall systems [29–31]. The second scenario is *chiral* channels, meaning that both spin species propagate in the same direction, as in the integer quantum Hall effect [32], so that backscattering is completely forbidden, and RKKY interactions cannot be generated. This has far reaching implications when combined with the multichannel Kondo effect, which is known (in the single-impurity case) to give rise to fractionalized quasiparticles due to frustration. These quasiparticles come with a fractional residual entropy [33], reminiscent of a single non-Abelian anyon, the exotic quasiparticles lying at the heart of topological quantum computing [34, 35]. In the multi-impurity case, the emergent RKKY interactions lift the frustration, thus avoiding fractionalization, but recent proposals try to circumvent this [36, 37]. As chirality eliminates the RKKY interactions, the decoupled non-Abelian anyons are expected to survive [37–39]. Recently the two- and three-channel Kondo effects have been demonstrated for a single quantum dot coupled to (multiple) integer quantum Hall (chiral) edge modes [40, 41], with clear signatures of the fractionalization [42–45]. Likewise, similar devices realizing two impurities have been studied [46]. Thus, one can expect that extending this setup to multiple impurities coupled by unidirectional chiral modes will enable experimental observation of decoupled anyons. We note that such an extension is more realistic with a *partially connected* scenario, where in one of the spin species the impurities are coupled to the same unidirectional channel, while in the other spin species each impurity is coupled to a separate channel.

It would therefore be useful to have a generic method for analyzing multiple quantum impurities coupled to the same unidirectional channel(s). For this we turn to Wilson’s numerical renormalization group (NRG) [47, 48], one of the most generic and reliable tools for studying quantum impurity models. A key part in (standard) NRG is mapping the electronic bath to a so-called Wilson chain—a tight-binding chain with the impurity at one end and hopping amplitudes decaying exponentially with the distance. Over the years, NRG has also been applied to two-impurity systems in different scenarios [15, 19, 21, 49–55] but always under the assumption of bidirectional channels, which enables mapping the bath to two separate Wilson chains, as illustrated in Fig. 1(b). Such a mapping is not possible for unidirectional channels, as a nearest-neighbor tight-binding chain has no notion of directionality.

Here we overcome this obstacle by mapping the bath to two coupled Wilson chains, or a *Wilson ladder*, as depicted in Fig. 1(c). We note that the resulting structure is formally a particular case of a channel mixing bath [56]. However, due to oscillatory terms which typically arise in two-impurity systems, the procedure introduced in Ref. [56] would face technical difficulties for a two-

impurity problem. Similar problems are also expected for a derivation based on open Wilson chains [57]. In this work, we therefore introduce an alternative derivation of the Wilson ladder. By exploiting PT (inversion + time reversal) symmetry, we enforce a real Hamiltonian, and together with particle-hole symmetry in the bath, we can nullify both onsite energies and crosslinks in the ladder. We then demonstrate that the Wilson-ladder structure correctly captures the distance between the two impurities, with a transition from two weakly coupled chains at high energies (or short wavelengths), to an effective single chain at low energies (or long wavelengths). Considering each ladder level as an enlarged effective site along a Wilson chain, we can proceed with iterative diagonalization by standard NRG procedure.

We test the mapping on two resonant levels coupled at different locations to a spinless chiral channel. Such a noninteracting system can be solved exactly both in the continuum limit (of the chiral channel) and after discretization, and so serves as an excellent benchmark for the method. We find that thermodynamic quantities are accurately captured at all temperatures, and that most features of zero-temperature spectral properties are also captured. However, some of the (exact) spectral quantities exhibit oscillations at a frequency corresponding to the interimpurity distance, which by construction cannot be captured by a logarithmic discretization procedure. Still, we find that we do successfully reproduce the envelope of the oscillations. This implies that static temperature-dependent correlation functions are successfully captured at low temperatures, while at high temperatures, for which the correlations should drop to zero exponentially, we get artificial oscillations around zero.

We then turn to study a single-channel chiral two-impurity Anderson model (in the local-moment limit). We find that by looking only at local impurity quantities, e.g., the impurity entropy and magnetic susceptibility, one cannot discern the difference between the chiral system and two separate copies of a single-impurity problem. Thus, at high temperatures, we have a free spin at each impurity, and at low temperatures both spins are fully screened, with the crossover (Kondo) temperature T_K independent of the distance between the impurities. This is actually consistent with the Bethe-ansatz solution of the Kondo problem [5, 6], which has also been applied to multiple impurities coupled to a chiral channel. It can also be explained by the following intuitive argument: Due to the absence of backscattering, the first impurity cannot “know” about the second, and thus “behaves” as in the single-impurity case. Applying a PT transformation, the same holds for the second (last) impurity. We point out that both in our solution, and implicitly in the Bethe-ansatz solution, one assumes some (possibly small) separation between the impurities. Thus, neither solution is applicable to two impurities exactly at the same point, but such a case is trivial, corresponding to an enlarged single-impurity problem, and is not the focus of this work. Looking at static impurity-impurity

correlations, we find that they do depend on the inter-impurity distance, and are nonzero at low temperatures. This is, however, expected—even in a trivial noninteracting chiral bath we have spatial correlations, and once the impurities are in the strongly-coupled regime, these correlations are reflected by the impurity-impurity correlations. Such *static* correlations do not affect the local impurity physics, and we demonstrate that a local perturbation at one impurity does not affect the local physics of the other, i.e., response functions (*retarded* correlations) are chiral.

The remainder of this paper will be ordered as follows: In Sec. II, we derive the Wilson ladder and comment about the NRG implementation, leaving some of the technical details to Appendices A and B. In Sec. III, we test the quality of this mapping on a noninteracting system, demonstrating its advantages and limitations; some technical details are relegated to Appendix C. We then apply the method to a spinful chiral channel coupled to two Kondo impurities in Sec. IV and analyze the results. Finally, we conclude in Sec. V and comment on possible applications of the presented method.

II. THE WILSON LADDER

We start this section by formally defining the problem we wish to address, pointing out where previous solutions break down, and setting the stage for the derivation of the Wilson ladder, which will then be outlined in the subsections. The Hamiltonian of a generic quantum impurity problem can be written as

$$H = H_{\text{imp}} + H_{\text{coupling}} + H_{\text{bath}}, \quad (1)$$

where H_{bath} describes a quadratic (noninteracting) fermionic bath, H_{imp} describes the (typically interacting) impurity degrees of freedom, and H_{coupling} couples the bath to the impurity(ies). In this section we will assume an Anderson impurity model, for which H_{coupling} is also quadratic. Wilson's NRG can be decomposed into three stages:

- A. *Logarithmic discretization*, or coarse graining, of the bath Hamiltonian.
- B. *Tridiagonalization* of the discrete bath Hamiltonian to a tight-binding (Wilson) chain with the impurity at one end.
- C. Numerical *iterative diagonalization* of the full Hamiltonian, probing ever shrinking energy scales with each iteration.

The first two steps are indifferent to the interaction U within the impurity sites [see Eq. (30) below]. Therefore, we set the impurity Hamiltonian to zero, perform the mapping, and reintroduce it only for the iterative diagonalization. Assuming the bath and coupling Hamiltonians are diagonal in spin and flavor indices, we can

apply the mapping to a single flavor of spinless fermions, and then duplicate the resulting structure. Thus, for the derivation of the Wilson ladder, we will consider a single channel of noninteracting spinless right-moving fermions coupled to two impurities at $\pm R/2$:

$$H_{\text{imp}} = 0, \quad (2a)$$

$$H_{\text{bath}} = \int_{-\infty}^{\infty} \psi^\dagger (-iv_F \partial_x) \psi dx, \quad (2b)$$

$$H_{\text{coupling}} = \tilde{t}_0 d_1^\dagger \psi \left(-\frac{R}{2}\right) + \tilde{t}_0 d_2^\dagger \psi \left(+\frac{R}{2}\right) + \text{H.c.}, \quad (2c)$$

where $\hbar=1$ throughout, v_F is the Fermi velocity, and we have assumed both impurities couple only locally and with equal real amplitude \tilde{t}_0 (but this can be generalized to more complicated setups). The fermionic field and impurity operators satisfy $\{\psi(x), \psi^\dagger(x')\} = 2\pi\delta(x-x')$ and $\{d_m, d_{m'}^\dagger\} = \delta_{mm'}$, respectively. Observe that Eq. (2) conserves total charge, and is invariant under the following transformations

$$\text{particle-hole} : \quad \psi(x) \rightarrow \psi^\dagger(x), \quad d_m \rightarrow -d_m^\dagger, \quad (3a)$$

$$\text{PT} : \quad x \rightarrow -x, \quad i \rightarrow -i, \quad d_1 \leftrightarrow d_2, \quad (3b)$$

but not under inversion or time reversal individually.

In order to point out where previous NRG approaches break down we will consider the impurities' retarded Green function, which can be written as a 2×2 matrix

$$\mathbf{G}^R(\omega) = [\omega \mathbf{1} - \mathbf{h} - \Sigma^R(\omega)]^{-1}, \quad (4)$$

with $\mathbf{1}$ the identity matrix, \mathbf{h} the (single-particle) impurity Hamiltonian, which in our case is zero, and

$$\Sigma^R(\omega) = \frac{\tilde{t}_0^2}{2iv_F} \begin{pmatrix} 1 & 2e^{i\omega R/v_F} \\ 0 & 1 \end{pmatrix}, \quad (5)$$

the retarded self-energy contribution due to hybridization with the bath. The zero element below the diagonal of Σ^R is the formal manifestation of chirality, which implies that a retarded quantity at $-R/2$ cannot depend on anything that happens at $+R/2$. This immediately carries on to $\mathbf{G}^R(\omega)$, as the inverse of an upper-triangular matrix is an upper-triangular matrix, and is not affected by the introduction of local potentials at the impurities or asymmetric couplings,

$$\mathbf{h} \rightarrow \begin{pmatrix} \mu_1 & 0 \\ 0 & \mu_2 \end{pmatrix}, \quad \Sigma^R(\omega) \rightarrow \frac{1}{2iv_F} \begin{pmatrix} |\tilde{t}_1|^2 & 2\tilde{t}_1 \tilde{t}_2^* e^{i\omega R/v_F} \\ 0 & |\tilde{t}_2|^2 \end{pmatrix}. \quad (6)$$

We define the impurity spectral function

$$\mathbf{A}(\omega) = -\frac{1}{2\pi i} [\mathbf{G}^R(\omega) - \mathbf{G}^A(\omega)], \quad (7)$$

with $\mathbf{G}^A = \mathbf{G}^{R\dagger}$. In Sec. III, we will test the quality of the discretization scheme by how well it reproduces $\mathbf{A}(\omega)$. An important consequence of the upper-triangular structure of $\mathbf{G}^R(\omega)$ is that the diagonal elements of the spectral function are equal to those of a single impurity with

the corresponding local potential and coupling. It is convenient to also define the hybridization function

$$\Gamma(\omega) = -\frac{1}{2i} [\Sigma^R(\omega) - \Sigma^A(\omega)] = \Gamma \begin{pmatrix} 1 & e^{i\omega R/v_F} \\ e^{-i\omega R/v_F} & 1 \end{pmatrix}, \quad (8)$$

where in the last form we returned to the case of symmetrically-coupled impurities, and defined $\Gamma \equiv \frac{t_0^2}{2v_F}$. As $\Gamma(\omega)$ encodes all the information about the bath, any bath which reproduces this hybridization function will result in the same impurity physics. NRG relies precisely on this property in order to replace the bath by a Wilson chain, to which we can apply iterative diagonalization.

Observe that $\Gamma(\omega)$ cannot be diagonalized by a frequency-independent transformation. This is the key difference between the unidirectional channel two-impurity models studied in this paper, and most bidirectional channel two-impurity models previously studied with NRG [15, 19, 21, 49–55]. For the latter, choosing an even-odd impurity basis diagonalizes the hybridization function, resulting in the impurities coupling to two separate channels, each of which can be mapped to a separate Wilson chain.¹ In our case, transforming to an even-odd (PT-symmetric) impurity basis

$$d_+ = \frac{1}{\sqrt{2}}(d_1 + d_2), \quad d_- = \frac{i}{\sqrt{2}}(d_1 - d_2), \quad (9)$$

results in a real hybridization function

$$\Gamma(\omega) \rightarrow \Gamma \begin{pmatrix} 1 + \cos\left(\frac{\omega R}{v_F}\right) & -\sin\left(\frac{\omega R}{v_F}\right) \\ -\sin\left(\frac{\omega R}{v_F}\right) & 1 - \cos\left(\frac{\omega R}{v_F}\right) \end{pmatrix}. \quad (10)$$

This guarantees a (numerically more stable and efficient) real representation for the discretized bath Hamiltonian, but clearly does not diagonalize $\Gamma(\omega)$. When the hybridization function cannot be diagonalized (by a frequency independent transformation), one can still take the approach by Liu *et al.* [56] and arrive at a generalized Wilson chain structure consisting of coupled chains. Introducing a 2-vector notation, $\mathbf{d} \equiv \begin{pmatrix} d_+ \\ d_- \end{pmatrix}$, $\mathbf{f}_n \equiv \begin{pmatrix} f_{n+} \\ f_{n-} \end{pmatrix}$, with $f_{n\pm}$ a discrete set of fermionic bath operators, our goal will be to write the coupling and bath Hamiltonians as

$$H_{\text{coupling}} = \mathbf{d}^\dagger \mathbf{T}_0 \mathbf{f}_0 + \text{H.c.}, \quad (11a)$$

$$H_{\text{bath}} = \sum_{n=0}^{2N} \mathbf{f}_n^\dagger \mathbf{E}_n \mathbf{f}_n + \sum_{n=0}^{2N-1} \mathbf{f}_n^\dagger \mathbf{T}_{n+1} \mathbf{f}_{n+1} + \text{H.c.}, \quad (11b)$$

where \mathbf{E}_n and \mathbf{T}_n are 2×2 coefficient matrices. Eqs. (11) resemble the expressions obtained in the standard Wilson

chain scheme for a single-impurity [48]. The difference is that fermionic operators and scalar coefficients are promoted to 2-vectors of operators, and scalar coefficients are promoted to 2×2 matrices. We will demonstrate that due to particle-hole symmetry in the bath, we can nullify the off-diagonal elements of \mathbf{T}_n and the diagonal elements of \mathbf{E}_n , resulting in a ladder structure, as depicted in Fig. 2(f).

In order to arrive at these expressions, we will first need to logarithmically discretize the Hamiltonian, bringing it into the so-called star geometry:

$$H_{\text{coupling}} = \sum_{n=\pm 1}^{\pm N} \mathbf{d}^\dagger \mathbf{V}_n \mathbf{c}_n + \text{H.c.}, \quad (12a)$$

$$H_{\text{bath}} = \sum_{n=\pm 1}^{\pm N} \mathbf{c}_n^\dagger \mathbf{E}_n \mathbf{c}_n, \quad (12b)$$

with \mathbf{c}_n being 2-vectors of fermionic operators, \mathbf{V}_n and \mathbf{E}_n coefficient matrices, and $4N$ the number of discrete modes. Note that apart from the introduction of a high-energy cutoff, Eq. (12a) will be exact, while writing the bath Hamiltonian as in Eq. (12b) is the main approximation in NRG. The discretization scheme used in Ref. [56] in order to obtain \mathbf{E}_n relies on separately diagonalizing the hybridization function $\Gamma(\omega)$ for each frequency and then proceeding as in Refs. [58, 59] to numerically solve a differential equation containing an integral over the diagonalized hybridization function. Due to the highly oscillatory structure of $\Gamma(\omega)$, we found this scheme to be ill suited for our case, and in Sec. II A, we will present an alternative (more traditional) discretization scheme which circumvents this. In Sec. II B, we will apply a generalized tridiagonalization procedure and arrive at the Wilson ladder of Eqs. (11), explicitly exploiting particle-hole symmetry. Finally, in Sec. II C, we will comment on several implementation details for the iterative diagonalization.

A. Logarithmic discretization

We will now outline a discretization procedure in terms of a general matrix hybridization function $\Gamma(\omega)$, with the goal of plugging Eq. (10) into the obtained expressions. However, one can equivalently discretize at the level of a specific continuous Hamiltonian, which for the chiral Hamiltonian in Eqs. (2) is very convenient. In Appendix A, we take this approach, as it allows for a clearer comparison with traditional discretization schemes, and specifically the derivation in Ref. [50], which we here generalize to a matrix hybridization.

In order to discretize the bath, we must first introduce a UV (high energy / short wavelength) cutoff D , typically related to the half-bandwidth. For a chiral model, e.g., an integer quantum Hall edge state, D is related to the bulk gap, and so $D/v_F \equiv k_{\text{max}}$ should not be associated with the Fermi wavevector k_F or an underlying lattice spacing. We point out that introducing this sharp

¹ The mapping of the bath onto two separate Wilson chains is possible as long as the impurities couple to two bath modes which are invariant under inversion $x \rightarrow -x$. This holds for typical bidirectional channels, but inherently breaks down in the unidirectional case.

cutoff, which is required for the numerics, breaks chirality, e.g., leading to a loss of orthogonality [which decays as $\text{sinc}(DR/v_F) \equiv \frac{\sin(DR/v_F)}{DR/v_F}$ —see Appendix A] between the two bath modes coupling to the real-space impurities d_1 and d_2 . We thus wish to stay in the large-bandwidth limit, i.e., D much larger than any relevant energy scale, so that the breaking of chirality is negligible. We can further negate these effects, improving numerical stability, by taking the cutoff to be commensurate with R , i.e.,

$$DR/v_F = k_{\max}R = \pi l ; l \in \mathbb{N}. \quad (13)$$

We then introduce a logarithmic discretization grid

$$\epsilon_1^z = D, \quad \epsilon_{n>1}^z = D\Lambda^{2-n-z}, \quad \epsilon_{n<0}^z = -\epsilon_{-n}^z, \quad (14)$$

where $\Lambda > 1$ controls the logarithmic level spacing and $z \in (0, 1]$ shifts the levels, upon which we define intervals

$$I_{n>0}^z = [\epsilon_{n+1}^z, \epsilon_n^z], \quad I_{n<0}^z = [-\epsilon_{-n}^z, -\epsilon_{-n-1}^z]. \quad (15)$$

In order to keep the notation compact, in what follows we will drop the z index, but remember it is implied whenever n appears.

Each impurity couples to a single mode in each interval. These two modes are generally not orthogonal with respect to each other, and in the continuum limit $\Lambda \rightarrow 1$ they actually coincide. However, for a finite Λ we can always choose linear combinations of the two which are orthonormal, to which we will refer as $\mathbf{c}_n = (\begin{smallmatrix} c_n^+ \\ c_n^- \end{smallmatrix})$. The coupling to these modes can be obtained by integrating over the hybridization function

$$[\mathbf{V}_n]^2 = \frac{1}{\pi} \int_{I_n} \mathbf{\Gamma}(\omega) d\omega. \quad (16)$$

As $\mathbf{\Gamma}(\omega)$ is a Hermitian positive matrix for each ω , so is its integral, which can thus be expressed as the square of some (Hermitian) matrix. Hence, its matrix square root \mathbf{V}_n and its inverse \mathbf{V}_n^{-1} are both well defined (and can be chosen to be Hermitian). Projecting the bath Hamiltonian onto the modes \mathbf{c}_n , we obtain the coefficient matrix

$$\mathcal{E}_n^{\text{naive}} = \pi \int_{I_n} d\omega \omega \mathbf{V}_n^{-1} \mathbf{\Gamma}(\omega) \mathbf{V}_n^{-1}. \quad (17)$$

As \mathbf{c}_n are not bath eigenmodes, this is where the main approximation in NRG enters.² Eqs. (16) and (17) generalize the standard (naive) single-impurity discretization

² This procedure can be understood as the expansion of the hybridization function in each interval I_n as a continued fraction, which is then truncated after one step, with the remaining continuum of states in the interval discarded following standard Wilsonian philosophy. See Ref. [57] for an outline of how to write down such an expansion for a hybridization function supported on some arbitrary interval, and specifically Appendix B therein, which demonstrates how to do so for a matrix hybridization function. Note a factor of π difference in the definition of our $\mathbf{\Gamma}(\omega)$ with respect to Ref. [57].

used in NRG [48] to a matrix hybridization. Following the notation of Ref. [59],³ one can immediately write the matrix generalization of the scheme by Campo and Oliveira [50] as

$$\mathcal{E}_n^{\text{CO}} = \left[\pi \int_{I_n} \frac{d\omega}{\omega} \mathbf{V}_n^{-1} \mathbf{\Gamma}(\omega) \mathbf{V}_n^{-1} \right]^{-1}. \quad (18)$$

In Appendix A, we formulate the derivation of \mathbf{V}_n , $\mathcal{E}_n^{\text{naive}}$ and $\mathcal{E}_n^{\text{CO}}$ (up to a unitary rotation) for our specific model in the language used in Ref. [50], explicitly demonstrating the source of the obtained expression.

We point out that for the PT-symmetric hybridization function of Eq. (10), the coefficient matrices are all real, and for positive and negative n (regardless of the discretization scheme) are related by

$$\mathbf{V}_{-n} = \sigma_z \mathbf{V}_{+n} \sigma_z ; \quad \mathcal{E}_{-n} = -\sigma_z \mathcal{E}_{+n} \sigma_z, \quad (19)$$

with $\sigma_z = (\begin{smallmatrix} 1 & 0 \\ 0 & -1 \end{smallmatrix})$. This is a manifestation of particle-hole symmetry, and will be exploited in the next section.

B. Tridiagonalization

In the single-impurity case, one has N positive-energy modes, N negative-energy modes, and one impurity mode, so that the single-particle Hamiltonian can be written as a $(2N+1) \times (2N+1)$ matrix. One can then numerically find a unitary transformation which brings it into tridiagonal form, e.g., by the Lanczos or Householder algorithms. This scheme can be readily generalized to the two-impurity case [56]: We now have $2N$ positive-energy modes, $2N$ negative-energy modes, and 2 impurity modes, so that the single-particle Hamiltonian can be written as a $(4N+2) \times (4N+2)$ matrix, or as a $(2N+1) \times (2N+1)$ block matrix with 2×2 elements \mathbf{V}_n and \mathcal{E}_n , as shown in Fig. 2(a). One can then apply a generalized Lanczos or Householder procedure in order to bring it to a block-tridiagonal form, as shown in Fig. 2(b). The Hamiltonian is thus given by Eqs. (11), which are rewritten here for the sake of clarity,

$$H_{\text{coupling}} = \mathbf{d}^\dagger \mathbf{T}_0 \mathbf{f}_0 + \text{H.c.}, \quad (20a)$$

$$H_{\text{bath}} = \sum_{n=0}^{2N} \mathbf{f}_n^\dagger \mathbf{E}_n \mathbf{f}_n + \sum_{n=0}^{2N-1} \mathbf{f}_n^\dagger \mathbf{T}_{n+1} \mathbf{f}_{n+1} + \text{H.c.}, \quad (20b)$$

with general matrices \mathbf{T}_n and Hermitian matrices \mathbf{E}_n . Since the coefficient matrices \mathbf{V}_n and \mathcal{E}_n obtained in the previous section (for a PT-symmetric hybridization) were all real, \mathbf{T}_n (\mathbf{E}_n) can be written as real (and symmetric) matrices. One still has the freedom to apply arbitrary unitary transformations to the 2×2 blocks. In the presence of particle-hole symmetry, these transformations can

³ See end of Appendix A for an explicit comparison with the notation of Ref. [59].

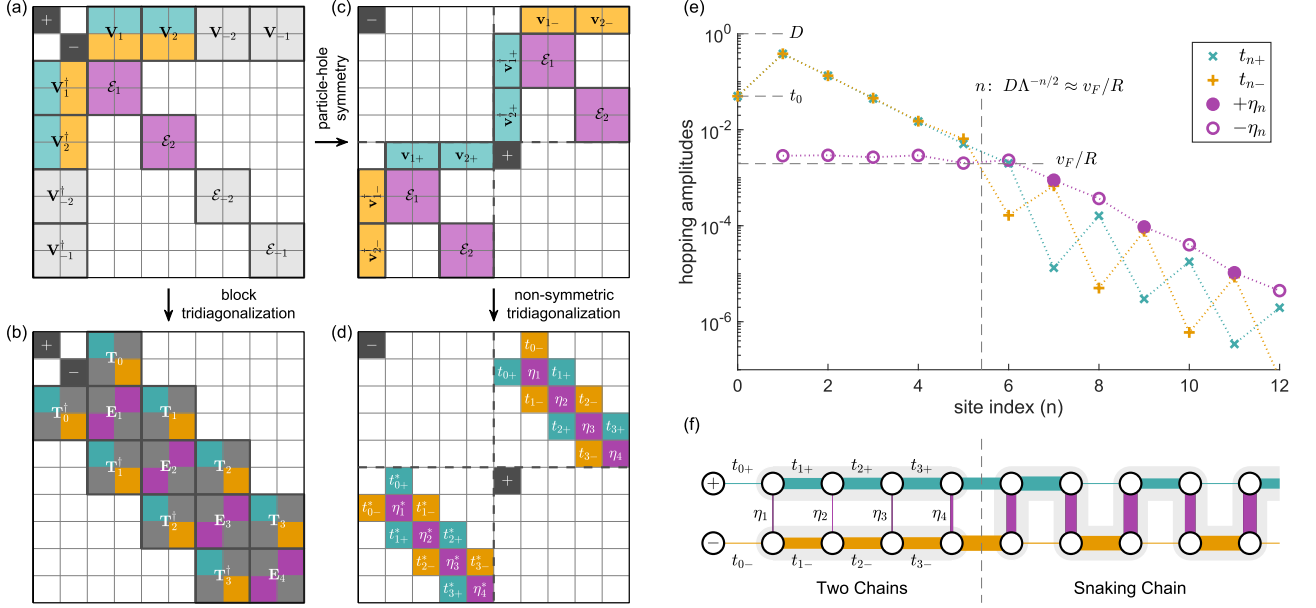


FIG. 2. (a) Block structure of the discretized Hamiltonian, corresponding to Eq. (12), with two positive and two negative energy intervals. White tiles are zero, and so are the black tiles, which indicate the location of the even (+) and odd (-) impurity modes. (b) Applying block tridiagonalization, one arrives at the generalized Wilson chain structure in Eqs. (20) [or Eqs. (11)]. White and black tiles are zero, and in the presence of particle-hole symmetry, the gray tiles can also be nullified, resulting in a Wilson ladder structure. (c) Transforming to a particle-hole symmetric basis, we get the structure in Eq. (23). Color-coding relates tiles of equal value between (a) and (c). Note that the indices of the even and odd impurity modes have changed. (d) Applying nonsymmetric tridiagonalization to the upper-right and lower-left quarters of (c) brings them to tridiagonal form. Color-coding relates tiles of equal value between (b) and (d). Note the alternating relation to even and odd hopping-amplitudes. (e) Hopping amplitudes along the Wilson ladder for an example case with $\Lambda = 9$, $z = 1$, $R/v_F = 2\pi\Lambda^2/D$, $t_0 = 0.05D$ ($2v_F/R \approx \Gamma \approx 0.004D$), with the different scales indicated on the graph by horizontal dashed lines. The vertical dashed line indicates the change in the qualitative behavior, which occurs when the hopping amplitudes cross the energy scale v_F/R . (f) Wilson ladder with link widths proportional to the value of the rescaled hopping amplitudes $t_{n\pm}\Lambda^{n/2}$, $\eta_n\Lambda^{n/2+1/4}$. The dashed line indicates the change from two weakly-coupled chains to a single snaking chain.

be used to nullify the diagonal terms in \mathbf{E}_n and the off-diagonal terms in \mathbf{T}_n , bringing us to the Wilson ladder structure shown in Fig. 2(f). This is a generalization to the zero onsite energies in the ordinary (single-impurity) Wilson chain in the presence of particle-hole symmetry. Here we present an alternative tridiagonalization procedure which exploits particle-hole symmetry, and thus by construction enforces the ladder structure.

The modes $\mathbf{c}_n = (c_{n+}^+, c_{n-}^-)^T$ do not respect particle-hole symmetry, meaning a particle-hole transformation mixes different such modes $\mathbf{c}_n \rightarrow \sigma_z [\mathbf{c}_{-n}^\dagger]^T$. However, we can take linear combinations \mathbf{a}_{n+} and \mathbf{a}_{n-} (introducing 4-vector notation),

$$\begin{pmatrix} \mathbf{a}_{n+} \\ \mathbf{a}_{n-} \end{pmatrix} = \frac{1}{\sqrt{2}} \begin{pmatrix} \mathbf{1} & \sigma_z \\ \mathbf{1} & -\sigma_z \end{pmatrix} \begin{pmatrix} \mathbf{c}_n \\ \mathbf{c}_{-n} \end{pmatrix}, \quad (21)$$

which transform as $\mathbf{a}_{n\pm} \rightarrow \pm [\mathbf{a}_{n\pm}^\dagger]^T$, and thus respect this symmetry. Together with the symmetry condition of Eq. (19), the bath and coupling Hamiltonians obtain

the form

$$H_{\text{coupling}} = \sum_{n=1}^N (d_+^\dagger \ d_-^\dagger) \sqrt{2} \begin{pmatrix} \mathbf{v}_{n+} & 0 & 0 \\ 0 & 0 & \mathbf{v}_{n-} \end{pmatrix} \begin{pmatrix} \mathbf{a}_{n+} \\ \mathbf{a}_{n-} \end{pmatrix} + \text{H.c.}, \quad (22a)$$

$$H_{\text{bath}} = \sum_{n=1}^N \begin{pmatrix} \mathbf{a}_{n+}^\dagger & \mathbf{a}_{n-}^\dagger \\ \boldsymbol{\varepsilon}_n & 0 \end{pmatrix} \begin{pmatrix} 0 & \boldsymbol{\varepsilon}_n \\ \boldsymbol{\varepsilon}_n & 0 \end{pmatrix} \begin{pmatrix} \mathbf{a}_{n+} \\ \mathbf{a}_{n-} \end{pmatrix}, \quad (22b)$$

where \mathbf{v}_{n+} and \mathbf{v}_{n-} are, respectively, the top and bottom rows of $\mathbf{V}_n = \begin{pmatrix} \mathbf{v}_{n+} \\ \mathbf{v}_{n-} \end{pmatrix}$.

We can now embed Eq. (22) into a single-particle Hamiltonian. We choose a seemingly peculiar order of rows (and columns): The first row corresponds to the odd impurity mode d_- , rows $2 \rightarrow 2N+1$ correspond to the particle-hole even bath modes \mathbf{a}_{n+} , row $2N+2$ corresponds to the even impurity mode d_+ , and rows $2N+3 \rightarrow 4N+2$ correspond to the particle-hole odd bath modes \mathbf{a}_{n-} . Thus, the single-particle Hamiltonian has the following structure

$$H = \begin{pmatrix} O & M \\ M^\dagger & O \end{pmatrix}, \quad M = \begin{pmatrix} 0 & \mathbf{v}_{1-} & \cdots & \mathbf{v}_{N-} \\ \mathbf{v}_{1+}^\dagger & \boldsymbol{\varepsilon}_1 & 0 & \cdots & 0 \\ \vdots & 0 & \ddots & \ddots & 0 \\ \vdots & 0 & \ddots & \ddots & 0 \\ \mathbf{v}_{N+}^\dagger & 0 & \cdots & 0 & \boldsymbol{\varepsilon}_N \end{pmatrix}, \quad (23)$$

as shown in Fig. 2(c), with M a $(2N + 1) \times (2N + 1)$ matrix and O a zeros matrix of the same dimension. M is not a Hermitian (symmetric, assuming real coefficients) matrix, but can still be brought to tridiagonal form by applying different unitary (orthogonal) transformations from the left and right

$$\mathcal{M} = U_+ M U_-^\dagger = \begin{pmatrix} 0 & t_{0-} & 0 & \cdots & 0 \\ t_{0+} & \eta_1 & t_{1+} & & \vdots \\ 0 & t_{1-} & \eta_2 & t_{2-} & 0 \\ \vdots & & t_{2+} & \eta_3 & \ddots \\ 0 & \cdots & 0 & \ddots & \ddots \end{pmatrix}, \quad (24)$$

with the labels of the matrix elements explained below. Then, specifying the unitary transformation $\mathcal{U} = \begin{pmatrix} U_+ & 0 \\ 0 & U_- \end{pmatrix}$ we can transform H into

$$\mathcal{U} H \mathcal{U}^\dagger = \begin{pmatrix} O & M \\ M^\dagger & O \end{pmatrix}, \quad (25)$$

as shown in Fig. 2(d). In the transformed Hamiltonian, rows 1 and $2N + 2$ still correspond to d_- and d_+ , respectively. If we identify rows $\begin{cases} n+2 & \text{even } n \\ n+3+2N & \text{odd } n \end{cases}$ with f_{n+} and rows $\begin{cases} n+3+2N & \text{even } n \\ n+2 & \text{odd } n \end{cases}$ with f_{n-} , we find that the elements of \mathcal{M} in Eq. (24) give us $\mathbf{T}_n = \begin{pmatrix} t_{n+} & 0 \\ 0 & t_{n-} \end{pmatrix}$ and $\mathbf{E}_n = \begin{pmatrix} 0 & \eta_n \\ \eta_n^* & 0 \end{pmatrix}$. Thus, we indeed get the ladder structure as advertised.

Let us study the obtained hopping amplitudes, which are plotted for an example case in Fig. 2(e). Without loss of generality we can choose real and positive ladder-rail amplitudes $t_{n\pm}$, and let any required phase fall on the rung amplitudes η_n . The latter are also real [due to the real coefficients in Eq. (12)], and so this phase amounts at most to a sign. Observe that the hopping amplitudes fall into two distinct regimes, separated by the energy scale corresponding to the interimpurity distance, v_F/R . This distinction is further emphasized in Fig. 2(f), in which the width of the different links corresponds to the hopping amplitudes when rescaled by $\Lambda^{-n/2}$.

Small values of n correspond to wavelengths shorter than the distance between the impurities, or conversely, impurities which are very far apart with respect to the wavelengths considered, so that we expect them to hardly affect each other. We indeed observe that the rail amplitudes decay exponentially $t_{n\pm} \sim \Lambda^{-n/2}$, with t_{n+} and t_{n-} of the same order for a given n , leading to two well-defined Wilson chains, while the rung amplitudes $\eta_n \approx v_F/R$ are constant and small, resulting in weak coupling between the chains, as depicted in the left part of Fig. 2(f). Thus, in the limit of extremely distant impurities $R \rightarrow \infty$, the chains completely decouple, as expected.

Large n correspond to wavelengths larger than the distance between the impurities, or conversely, impurities which are very close to each other. In the limit $R \rightarrow 0$, we expect both impurities to couple to the same bath mode,

resulting in a single Wilson chain.⁴ Indeed, we observe that both the rail and the rung amplitudes decay exponentially $\sim \Lambda^{-n/2}$, but we have alternating weak rail amplitudes, and rung amplitudes which are of order of the strong rail, as depicted in the right part of Fig. 2(f). This corresponds to a single Wilson chain snaking through the ladder, with small next-next-nearest-neighbor corrections. Note that this snaking chain has two sites for each n . Thus, renumbering the sites along the snake by index m , we see that the hopping amplitudes decay along the effective chain as $\sim \sqrt{\Lambda}^{-m/2}$, which can be interpreted as an effective smaller logarithmic discretization parameter $\sqrt{\Lambda}$ in this regime. Note also that although this has no consequences, one can get a slightly cleaner picture by transferring the alternating signs of the rung amplitudes to the weak links, so that all weak links are negative, and the snaking chain has positive amplitudes.

Before moving on, we return to shortly discuss the freedom of applying arbitrary 2×2 unitary rotations u_n between the two modes at each level of the ladder (defining $\mathbf{f}_{-1} \equiv \mathbf{d}$ as the impurity modes)

$$\mathbf{f}_n \rightarrow u_n^\dagger \mathbf{f}_n, \quad \mathbf{E}_n \rightarrow u_n^\dagger \mathbf{E}_n u_n, \quad \mathbf{T}_n \rightarrow u_{n-1}^\dagger \mathbf{T}_n u_n. \quad (26)$$

Setting $\mathbf{E}_n = \eta_n \sigma_x$ and $\mathbf{T}_n = \frac{t_{n+} + t_{n-}}{2} \mathbf{1} + \frac{t_{n+} - t_{n-}}{2} \sigma_z$ with real coefficients, we have fully utilized this freedom (up to signs), and this comes naturally in the construction of Eq. (22b) [or Figs. 2(c) and 2(d)]. However, we can return to the block-tridiagonal structure in Fig. 2(b) and play with the u_n rotations, investigating their effect on the Wilson ladder. An immediate observation is that if we wish to retain zero onsite energies, we can modify the phases of the ladder rungs, but not their amplitudes. We can also take the impurities back to the real-space basis by inverting Eq. (9), i.e., choosing $u_{-1} = u \equiv \frac{1}{\sqrt{2}} \begin{pmatrix} 1 & 1 \\ i & -i \end{pmatrix}$:

$$\mathbf{d} = \begin{pmatrix} d_+ \\ d_- \end{pmatrix} \rightarrow u^\dagger \mathbf{d} = \frac{1}{\sqrt{2}} \begin{pmatrix} 1 & -i \\ 1 & i \end{pmatrix} \begin{pmatrix} d_+ \\ d_- \end{pmatrix} = \begin{pmatrix} d_1 \\ d_2 \end{pmatrix}. \quad (27)$$

This comes at the cost of a nondiagonal and complex \mathbf{T}_0 , compromising the ladder structure. However, we can proceed to choose $u_0 = u$, transforming the first ladder sites \mathbf{f}_0 to the real-space basis, resulting in purely imaginary rung hopping amplitudes (of magnitude η_0), and, assuming equal rails $t_{0+} = t_{0-}$, regaining the diagonal structure of \mathbf{T}_0 . Now the next level has cross terms, but as long as we have equal rails, $t_{n+} = t_{n-}$, i.e., at the earlier levels of the ladder, as demonstrated in Fig. 2(e), sequentially applying $u_n = u$ will preserve the ladder structure

⁴ One has to be careful with the order of limits with respect to the high-energy cutoff D . We assume $R \gg v_F/D$, which even in the limit of small R (and $D \rightarrow \infty$) retains a finite short chiral wire segment between the two impurities, such that inversion and time reversal symmetry remain independently broken (but PT is conserved). This assumption is also implied, although not explicitly stated, in the multi-impurity Bethe-ansatz solution.

(with purely imaginary rungs). Once we arrive at the snaking regime, where $t_{n+} \neq t_{n-}$, such transformations will start compromising the ladder structure. However, in that regime, it is indeed more natural to remain in the even-odd basis, with both impurities coupling to the even mode, and the odd mode (approximately) decoupling, resulting in a single chain.

As a final note, we mention that the entire procedure is quite sensitive to the oscillations in the hybridization function, and in order to retain double-precision ($\sim 10^{-16}$) accuracy in the Wilson ladder couplings, we had to resort to higher precision arithmetics (with $\sim 10^{-32}$ accuracy), both in the discretization, i.e., in the evaluation of Eqs. (16)–(18), as well as in the tridiagonalization. Once the Wilson ladder is obtained, the couplings can be cast back to double precision, with the numerical iterative diagonalization performed at that level.

C. Iterative diagonalization

In Sec. IV, we will reintroduce interactions at the impurities, so that the system can no longer be solved in the single-particle basis. Thus, we will need to proceed with iterative diagonalization. As this is standard NRG procedure, we only give a quick overview for completeness, and refer the reader to Refs. [48, 60] for further details. We then comment on several points which proved important in the implementation for our specific problem.

The challenge which the iterative diagonalization procedure comes to address is the exponential scaling of the Hilbert space size with the number of bath (and impurity) modes, so that full exact diagonalization is feasible only for very small systems. However, thanks to the logarithmic discretization, we can use the low-energy spectrum of a finite Wilson chain (or ladder) of length n' in order to calculate the low-energy spectrum of a chain (or ladder) of length $n' + 1$. Thus, we start with a short chain, which we can fully diagonalize, (i) keep only a fixed number N_K of low-energy states, (ii) add a new site, enlarging the considered Hilbert space, (iii) diagonalize the new Hamiltonian, and return to step (i), proceeding iteratively to construct a chain of any desired length, while for each chain length we have only a fixed number, N_K , of low-energy states. The reason this works is the exponential decay of the hopping amplitudes along the chain, which induces energy scale separation, i.e., the coupling of site $n' + 1$ to site n' serves only as a small perturbation to a chain of length n' . Thus, it can only mix states of similar energy, implying that the N_K low-energy states of a chain of length $n' + 1$ indeed only depend on states already contained in the N_K low-energy states of the chain of length n' . We therefore obtain an effective low-energy Hamiltonian for any desired energy scale (or chain length), and the iterative diagonalization is really a numerical implementation of a renormalization group flow from high to low energies (or temperatures). We can then track the changes in the effective Hamiltonians

in order to identify fixed points, and also extract thermodynamic and (zero or finite temperature) static and dynamical quantities.

When dealing with two-impurity problems (also in the bidirectional case), each channel is mapped to two effective channels (odd and even). As the computational cost of NRG, i.e., the required number of kept states, N_K , for a desired precision, scales exponentially with the number of channels, this proves a major challenge. When the different channels are decoupled, as in single-impurity-multichannel or two-impurity-bidirectional-channel calculations, one can interleave the different channels [61, 62], introducing each new site channel by channel, and reducing the number of states back to N_K after each channel. In order to preserve energy scale separation after the introduction of each channel, the different channels must be shifted with respect to each other by a channel-dependent z shift. However, once the channels are coupled, as in our case, it is not clear how to introduce this shift. Thus, in each iteration we must introduce the even and odd channels, i.e., the two ladder sites at the new level, together.

The computational cost can also be reduced significantly by exploiting different symmetries. The interacting model considered in this paper (in Sec. IV) exhibits $SU(2)_{\text{charge}} \otimes SU(2)_{\text{spin}}$ symmetry, with the former due to charge conservation together with particle-hole symmetry. As we use the contemporary formulation of NRG as a matrix-product-state algorithm [60], exploiting these symmetries can be delegated to the underlying tensor-network library, in our case QSPACE [60, 63, 64], which treats Abelian and non-Abelian symmetries on equal footing. This requires formulating the problem (e.g., the Hamiltonian) in terms of operators which respect the symmetry. It is usually straightforward, but in our case incurs several technical issues, which are addressed in Appendix B. The considered model is also PT symmetric, and so when written in terms of PT-symmetric fermionic operators (as discussed in the Sec. II B for the Wilson ladder and in Appendix B for the interaction terms), must have real coefficients. As the fermionic operators themselves can also be written as real tensors, we can resort to real (double-precision) arithmetics, which result in a factor of ~ 4 speedup with respect to complex (double-precision) arithmetics.

III. NONINTERACTING BENCHMARK

We can now test the quality of the presented mapping by looking at how well it reproduces the chiral behavior in the exactly-solvable noninteracting case. Note that the tridiagonalization procedure in Sec. II B is exact, and the iterative diagonalization in Sec. II C can in principle be brought to any desired accuracy. Thus, we are only testing the quality of the discretization presented in Sec. II A, and calculate all quantities from the single-particle Hamiltonian (see Appendix C). However, the re-

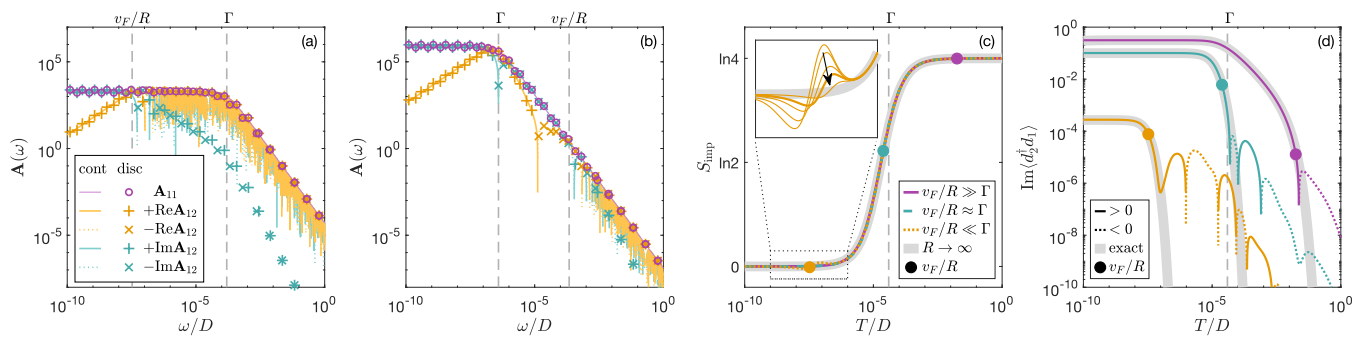


FIG. 3. Comparison of the Wilson-ladder numerical discretization (with $\Lambda = 3$) and the analytical continuum limit for a noninteracting two-impurity model. (a,b) The elements of the impurity spectral function matrix for $3.3 \times 10^{-8}D = v_F/R \ll \Gamma = 1.5 \times 10^{-4}D$ and $2.2 \times 10^{-4}D = v_F/R \gg \Gamma = 3.9 \times 10^{-7}D$, respectively, taking $z = 1$. The continuum limit result according to Eq. (28) is indicated by solid (dotted) lines for positive (negative) values, and discrete system results are indicated by the different markers. (c) The impurity entropy is plotted as a function of temperature for fixed $\Gamma \approx 4 \times 10^{-5}D$ ($t_0 = 0.005D$) and various finite distances R (with v_F/R indicated by circles) as well as $R \rightarrow \infty$ (shaded gray), averaged over four z shifts. The inset demonstrates the elimination of a numerical artifact at $v_F/R \ll \Gamma$ upon reducing the logarithmic discretization parameter $\Lambda = 9, 6, 4, 3, 2$. (d) Imaginary part of the temperature-dependent static impurity-impurity correlator for the same parameters as in (c), calculated after discretization. The continuum limit results (shaded gray) for the same distances are plotted as a reference.

sults have a clearer interpretation when considering the structure of the Wilson ladder. Assuming the large bandwidth limit, i.e., the high-energy cutoff D much larger than all other scales, we are left with two characteristic energy scales in the problem: the inverse interimpurity distance v_F/R , and $\Gamma = \frac{t_0^2}{2v_F} = \frac{\pi t_0^2}{2D}$, which quantifies the hybridization strength, and plays the role of the Kondo temperature in the noninteracting limit.

We start by comparing the continuum-limit expression for the impurity spectral function with its discrete version. In the limit $D \rightarrow \infty$ (while keeping Γ and v_F/R finite), the spectral function is given by Eq. (7), with its components rewritten here explicitly

$$\mathbf{A}_{11}(\omega) = \mathbf{A}_{22}(\omega) = \frac{\Gamma/\pi}{\omega^2 + \Gamma^2}, \quad (28a)$$

$$\mathbf{A}_{12}(\omega) = \mathbf{A}_{21}^*(\omega) = \frac{\Gamma/\pi}{\omega^2 + \Gamma^2} \frac{\omega - i\Gamma}{\omega + i\Gamma} e^{i\omega R/v_F}. \quad (28b)$$

Observe that the diagonal elements (which are real by construction) are equal, $\mathbf{A}_{11}(\omega) = \mathbf{A}_{22}(\omega)$, independent of R , and equal to the spectral function of a single-impurity resonant-level model (i.e., the $R \rightarrow \infty$ limit). This is a key signature of chirality, and any local perturbation, e.g., an onsite potential or different coupling t_0 , at either of the impurities will not affect the other impurity [i.e., its spectral function—see discussion around Eq. (6)]. The discrete version of the spectral function can be evaluated at the single-particle eigenenergies, with its different unique components plotted in Figs. 3(a) and 3(b) for $v_F/R \ll \Gamma$ and $v_F/R \gg \Gamma$, respectively. The diagonal (local) elements are correctly captured at all energy scales, as indicated by the circles. The off-diagonal elements are trickier: Their magnitude follows the same Lorentzian as the diagonal terms and is correctly captured at all scales, but they also have a phase, which for $\omega < v_F/R$

is correctly captured, but for $\omega \gg v_F/R$ is highly oscillatory, and thus cannot be captured by the logarithmic discretization.

We then turn to consider the impurity contribution to the entropy $\mathcal{S}_{\text{imp}} \equiv \mathcal{S} - \mathcal{S}_0$, defined as the difference between \mathcal{S} , the entropy of the full system, and \mathcal{S}_0 , the entropy of the bath when decoupled from the impurity. In Fig. 3(c), we plot \mathcal{S}_{imp} as a function of temperature (taking $k_B = 1$) for different interimpurity distances R . Let us first examine the $R \rightarrow \infty$ limit (gray), which corresponds to two copies of single-impurity models, so that the impurity entropy is additive. At high temperatures the two impurities are effectively decoupled from the system, so that each can be either full or empty, yielding four possible impurity configurations, resulting in $\mathcal{S}_{\text{imp}} = \ln 4$. At low temperatures each impurity is strongly coupled to the bath, so that there are no free impurity degrees of freedom and we have $\mathcal{S}_{\text{imp}} = 0$. The transition between the two regimes naturally occurs at the scale Γ . Going to finite R , with v_F/R larger (solid purple), smaller (dotted orange), and of order (dashed green) of Γ , we observe that as long as v_F/R is far below the cutoff, \mathcal{S}_{imp} is completely independent of R . Thus, the $R \rightarrow \infty$ behavior in fact holds for arbitrary distances between the impurities, and we expect it to apply for any (global) impurity thermodynamic property. Note that for $v_F/R < \Gamma$, a kink appears in the entropy at $T \sim v_F/R$, as shown in the inset. However, this kink, which will also appear in the interacting case when $v_F/R < T_K$, is a numerical artifact, and disappears upon shrinking Λ .

Lastly we turn to consider the thermal correlation

functions between the impurities' fermionic operators:

$$\begin{aligned} \langle d_m^\dagger d_m \rangle_T &= \frac{1}{\beta} \sum_{i\nu_l} \mathbf{G}_{mm'}(i\nu_l) e^{i\nu_l 0^+} \\ &= \int_{-\infty}^{\infty} \mathbf{A}_{mm'}^{(T=0)}(\omega) f_{\text{FD}}(\omega; T) d\omega, \end{aligned} \quad (29)$$

where $\mathbf{G}(i\nu_l) = \begin{cases} \mathbf{G}^R(i\nu_l) & \nu_l > 0 \\ \mathbf{G}^A(i\nu_l) & \nu_l < 0 \end{cases}$ is the Matsubara Green function, with $\nu_l = (2l+1)\pi/\beta$ the fermionic Matsubara frequencies and $\mathbf{G}^R = \mathbf{G}^{A\dagger}$ given by Eq. (4). In the second line, \mathbf{A} is the zero temperature spectral function, and the temperature dependence enters only through the Fermi-Dirac distribution, f_{FD} . From symmetry considerations we expect both impurities to be at half-filling, i.e., $\langle d_m^\dagger d_m \rangle_T = \frac{1}{2}$ for all temperatures, and this is indeed reproduced (not shown). Thus, the only relevant information appears in the off-diagonal terms, which are evaluated numerically both in the continuum limit and for the discrete system. We find that at temperatures $T < v_F/R$ the correlations are captured correctly by the discrete system. However, as is evident from the second line of Eq. (29), the oscillations in the spectral function impair the high-temperature results, which should fall exponentially, but instead oscillate around zero, decaying at a slower rate.

Before moving to the interacting case, we draw the main conclusions from this section. Our scheme reliably reproduces the thermodynamics, as well as local dynamics, but its validity regarding interimpurity properties depends on the interimpurity distance. As one would have expected, the discretized NRG scheme does not reproduce the fast oscillations at energies exceeding v_F/R . However, these high-energy discrepancies are washed out as one looks at low energies, where the spectral functions are accurately reproduced. Most importantly, these discrepancies do not compromise chirality, which is preserved on all energy scales, as demonstrated by the distance independence of the thermodynamic and local spectral quantities at all energy scales.

IV. CHIRAL TWO-IMPURITY KONDO MODEL

We are now ready to proceed to a spinful system and introduce local Coulomb interactions at each impurity. We start with a two-impurity Anderson model

$$H_{\text{imp}} = \sum_{m=1,2} [\varepsilon_d (n_{m\uparrow} + n_{m\downarrow}) + U n_{m\uparrow} n_{m\downarrow}], \quad (30)$$

where $n_{m\sigma} = d_{m\sigma}^\dagger d_{m\sigma}$ is the occupation operators of impurity m , and H_{coupling} and H_{bath} are as in Eq. (2) with the introduction of spin indices. In order to restrict the parameter space, in this work, we focus on the particle-hole symmetric regime, $\varepsilon_d = -U/2$, and take the local-moment limit $U \gg \Gamma$. Thus, each impurity retains a spin-half degree of freedom \tilde{S}_m , and, employing a Schrieffer-Wolff transformation [65], we arrive at the two-impurity

chiral Kondo model, with H_{bath} as before and

$$H_{\text{imp}} + H_{\text{coupling}} = J\tilde{S}_1 \cdot \tilde{s}\left(-\frac{R}{2}\right) + J\tilde{S}_2 \cdot \tilde{s}\left(+\frac{R}{2}\right), \quad (31)$$

where $\tilde{s}(x) = \frac{1}{2} \sum_{\sigma\sigma'} \psi_\sigma^\dagger(x) \vec{\sigma}_{\sigma\sigma'} \psi_{\sigma'}(x)$ is the bath spin operator at position x , $\vec{\sigma} = (\sigma_x, \sigma_y, \sigma_z)$ are the Pauli matrices, and $J = \frac{16}{\pi} D\Gamma/U = 8t_0^2/U$ is the Kondo coupling.⁵ H_{bath} is unaffected by the Schrieffer-Wolff transformation, and can still be mapped to the Wilson ladder in Eq. (11b). Note that the interaction terms of both models, as defined above, are invariant under both inversion and time reversal, and so the full Hamiltonian is still PT symmetric.

As a baseline we consider infinitely spaced impurities, i.e., $R \rightarrow \infty$, in which case the system corresponds to two separate copies of a single-impurity Kondo (or Anderson) model. Each copy undergoes a regular Kondo effect, with each spin fully screened at temperatures below the Kondo temperature

$$T_K = D\sqrt{\rho J} \exp\left(-\frac{1}{\rho J}\right), \quad (32)$$

where $\rho = \frac{1}{2D}$ is the local bath density of states (at the Fermi energy). Thus, whenever we refer to the $R \rightarrow \infty$ limit, we actually run a standard NRG calculation for the single-impurity problem, and multiply results by 2 (due to the two impurities) when necessary. In what follows, we then hold the single-impurity Kondo temperature T_K fixed, and introduce a finite interimpurity separation R .

We start with global thermodynamic quantities: The magnetic susceptibility $\chi_{\text{imp}} \equiv \chi - \chi_0$ (multiplied by temperature) in Fig. 4(a) and the impurity entropy $\mathcal{S}_{\text{imp}} \equiv \mathcal{S} - \mathcal{S}_0$ in Fig. 4(b), both defined as the difference between the thermodynamic quantity of the full system (\mathcal{S} or χ) and that of a decoupled bath (\mathcal{S}_0 or χ_0). Observe that for all R they follow the universal curve of the single-impurity spin- $\frac{1}{2}$ Kondo effect (for each impurity, so multiplied by 2 for both, in shaded gray): At high temperatures we have a free spin at each impurity, resulting in $\mathcal{S}_{\text{imp}} = \ln 4$ entropy and $T\chi \rightarrow \frac{1}{2}$ ($\mathcal{S}_{\text{imp}} = \ln 2$ and $T\chi \rightarrow \frac{1}{4}$ per impurity), while at low temperatures we go to the strong coupling fixed point, where the spins are fully screened, with no residual impurity degrees of freedom, resulting in zero entropy and $T\chi \rightarrow 0$. We can further probe the additivity of global quantities by breaking the symmetry between the impurities, so that each is expected to contribute differently to the global quantities. In Fig. 4(c), we introduce impurity-dependent Kondo couplings J_1 and J_2 , breaking only PT symmetry but retaining all other symmetries. In Fig. 4(d), we retain equal couplings but introduce a magnetic field B at

⁵ In practice we employ a useful NRG trick: Instead of implementing the (two-impurity) Kondo Hamiltonian, we use the (two-impurity) Anderson Hamiltonian, setting $U \gg \Gamma \gg D$, which numerically implements the Schrieffer-Wolff transformation.

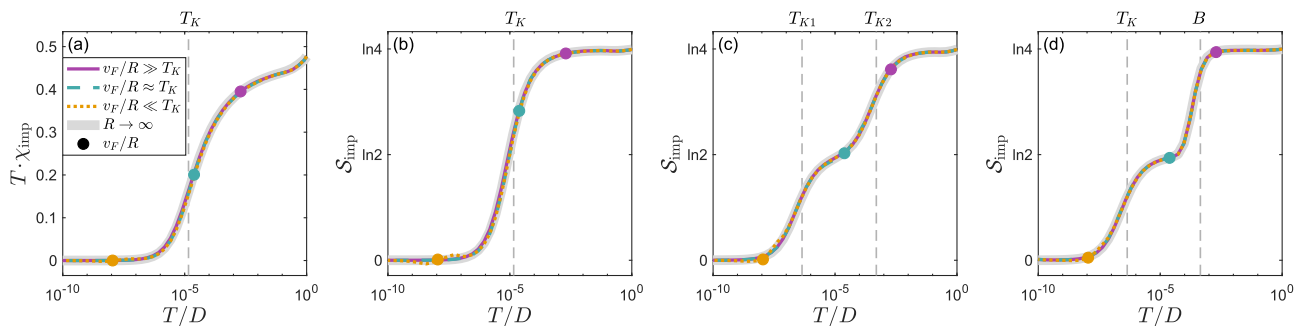


FIG. 4. Distance independence of thermodynamic properties of the chiral two-impurity Kondo model. The Kondo coupling J is fixed, with the corresponding T_K indicated by a dashed line. The interimpurity distance is taken at three typical values $DR/v_F = 2\pi\Lambda^4$ (purple) $2\pi\Lambda^8$ (green), $2\pi\Lambda^{15}$ (orange) and in the $R \rightarrow \infty$ separate-impurities limit (shaded gray), with $\Lambda = 3$, up to 5000 kept multiplets, and a single z shift $z = 1$. (a) Impurity magnetic susceptibility multiplied by temperature and (b) Impurity entropy with equal couplings $J/D = 0.2$; (c) Impurity entropy with impurity-dependent couplings $J_1/D = 0.15$ and $J_2/D = 0.3$; (d) Impurity entropy with equal couplings $J/D = 0.15$ and a magnetic field $B = 1000T_K$ only at the second impurity.

one impurity (results are indifferent to which impurity), thus breaking both $SU(2)_{\text{spin}}$ and PT symmetry. In both cases the resulting impurity entropy is simply the sum of two single-impurity models (shaded gray), either with different couplings, or with different magnetic fields (0 and B).

We thus arrive at the conclusion that the local physics of each impurity is indifferent to the distance between the impurities (also for $T \ll v_F/R$), and each undergoes a single-impurity Kondo effect. Although initially surprising, this is consistent with the Bethe ansatz [5],⁶ which also accounts for multiple impurities connected to a chiral channel, and actually has an intuitive explanation: Due to chirality, electrons cannot backscatter, and thus can only forward scatter first off the first impurity and then off the second, at most acquiring a phase shift at each impurity. However, nothing in this description depends on the distance between the impurities, and so each impurity contributes a $\frac{\pi}{2}$ phase shift just as in the $R \rightarrow \infty$ limit, resulting in a global π phase shift, regardless of the distance. In a more colloquial language, the first impurity does not “know” about the second impurity, so that from its perspective this is a single-impurity problem, and from PT symmetry the same holds for the second (last) impurity.

In order to appreciate these results, we first recall the paradigmatic Doniach [13] scenario for the bidirectional case. There, for finite separation between the impurities, the bath can mediate effective RKKY [10–12] interactions between the two impurities, i.e., $K(R) \vec{S}_1 \cdot \vec{S}_2$, which can be either ferromagnetic ($K < 0$) or antiferromagnetic ($K > 0$), driving the two impurities towards an impurity-impurity triplet or singlet, respectively. This competes

with the Kondo effect, which drives each impurity towards a singlet with a collective bath mode in its vicinity. Due to the finite distance between the impurities, a single bath generically provides two effective Kondo screening channels, e.g., even and odd. Thus, in the case of ferromagnetic interaction (or weak enough antiferromagnetic interaction), one gets a fully Kondo-screened triplet, while for strong antiferromagnetic interaction one gets a self-screened interimpurity singlet, which requires no further Kondo screening [15, 21].⁷ The two-impurity chiral model, however, clearly does not adhere to this picture, as demonstrated, e.g., by the impurity entropy in Fig. 4, which shows that:

- (i) The two impurities are fully screened, as $\mathcal{S}_{\text{imp}}^{T \rightarrow 0} \rightarrow 0$.
- (ii) The screening mechanism is of Kondo nature, as it occurs at T_K for all interimpurity distances.

Point (i) rules out an interimpurity triplet, as, in contrast to a bidirectional channel, a chiral channel cannot provide two independent screening channels; hence, if a triplet were to form, it would remain under-screened. The antiferromagnetic interimpurity correlations (to be discussed below) in Fig. 5(a) also contradict such a

⁶ The interimpurity distance does not appear explicitly in the Bethe-ansatz solution, but finite separation between the impurities is assumed implicitly by taking the large bandwidth (or continuous channel) limit.

⁷ There are exceptions to this rule, e.g., if one of the screening channels decouples (at low or all temperatures), so that for ferromagnetic RKKY we are left with an under-screened triplet. One such example is in the limit of vanishing interimpurity distance $R \ll v_F/D = 1/k_{\text{max}}$ (for an arbitrary dispersion), so that the two impurities are effectively at the same site, and thus couple to the same single (even) screening channel. Another example is a 1D bidirectional channel with interimpurity distances R that are commensurate with the high-energy cutoff, i.e., integer $k_{\text{max}}R/\pi$ [53], which for a linearized dispersion at half-filling (so that $k_{\text{max}} = k_F$) corresponds to impurities that are separated by an even number of lattice spacings. Note that this condition differs from the one in Eq. (13), since for a chiral channel k_{max} is not associated with k_F and the underlying lattice spacing.

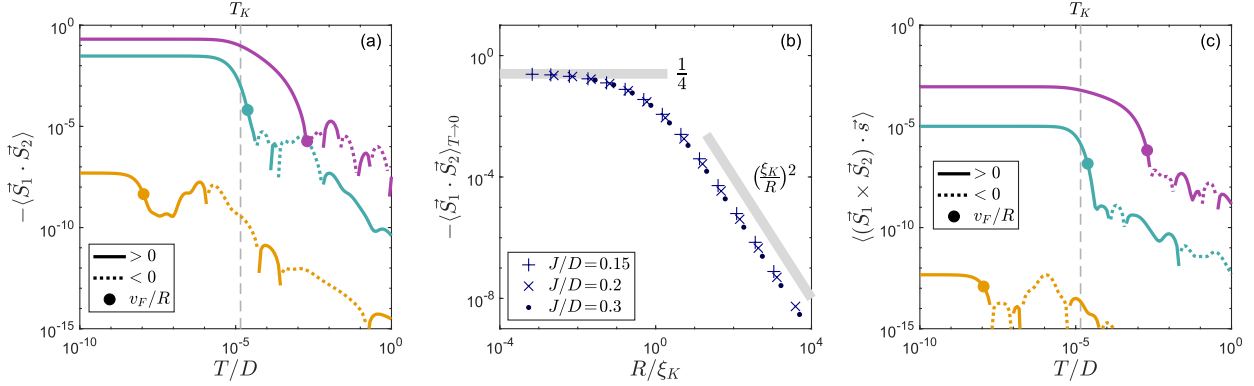


FIG. 5. Static temperature-dependent correlations for the chiral two-impurity Kondo model with the same parameters as in Fig. 4 (unless stated otherwise), and averaged over four z shifts: (a) Temperature-dependent impurity-impurity correlations; (b) $T \rightarrow 0$ impurity-impurity correlations for different Kondo-couplings J as a function of the interimpurity distance R rescaled by the Kondo length scale $\xi_K \equiv v_F/T_K$; (c) Temperature-dependent chiral correlations which violate both inversion and time reversal symmetry, but not their product PT symmetry.

triplet. Point (ii) rules out a self-screened RKKY singlet, which would be expected to form at the RKKY energy scale $K(R)$. The absence of any distance-related scale in all local quantities suggests that such effective interactions indeed do not emerge. However, this is to be expected, as chirality prevents the emergence of RKKY interactions.

We are thus left with the question: What are the consequences of both impurities being coupled to the same (chiral) bath? In order to address it, we need to consider nonlocal quantities, and thus turn to static temperature-dependent correlations between the impurities, starting with $\langle \tilde{S}_1 \cdot \tilde{S}_2 \rangle_T$ in Fig. 5(a). At high temperatures we observe only numerical noise, which is both positive and negative. However, once we reach temperatures $T < v_F/R$, antiferromagnetic (negative) correlations set in. Observe that the magnitude of the correlations becomes substantial (with respect to its $T \rightarrow 0$ value) once $T < T_K$, i.e., in the strong coupling regime. The $T \rightarrow 0$ value of these correlations is plotted in Fig. 5(b) as a function of the interimpurity distance R and for different Kondo couplings J . We find it to be a function of a single parameter R/ξ_K , with $\xi_K \equiv v_F/T_K$ the single-impurity Kondo length scale (which is inevitable, as this is the only remaining scale in the regime $T \rightarrow 0$, $T_K, v_F/R \ll J, D$). For large separation, the correlations decay as R^{-2} , while for interimpurity distance smaller than ξ_K they saturate to a constant, which, curiously, appears to be $-\frac{1}{4}$, the strongest possible correlation in the absence of interimpurity entanglement (meaning the two-impurity density matrix remains separable [66]). In Fig. 5(c), we plot a chiral correlation $\langle (\tilde{S}_1 \times \tilde{S}_2) \cdot \tilde{s} \rangle_T$ with $\tilde{s} = \tilde{s}(-R/2) + \tilde{s}(+R/2)$, which follows a similar trend to $\langle \tilde{S}_1 \cdot \tilde{S}_2 \rangle_T$. The interesting property of this quantity is that its average usually must vanish, as it breaks both inversion and time reversal symmetry separately. However, it does not break the product of the two symmetries,

i.e., PT symmetry, and is thus allowed to be finite in the chiral case.

It should be stressed that the observed correlations do not imply effective interactions, nor bidirectional causality between the impurities. Indeed, for temperatures lower than v_F/R a (noninteracting) chiral channel exhibits static correlations between $\psi(-R/2)$ and $\psi(+R/2)$, even though an event at $+R/2$ cannot affect $\psi(-R/2)$ [see the chiral structure of $\Sigma^R(\omega)$ in Eq. (5)]. These correlations decay as $\sim R^{-1}$, resulting in $\sim R^{-2}$ decay of the bath spin-spin correlations. Once the Kondo effect sets in, the impurity spins fuse into the bath, so that the bath correlations are reflected onto the impurity-impurity correlations. This onset of the correlations at T_K is clearly demonstrated in Fig. 5(a), and the $\sim R^{-2}$ decay of their $T \rightarrow 0$ value in Fig. 5(b) matches that of the bath. The saturation to the constant $-\frac{1}{4}$ at short distances can also be understood in this picture: The collective bath spins to which the impurities fuse have a finite size, ξ_K , and so for distances $R < \xi_K$, they are highly correlated, resulting in the two impurity spins also becoming maximally correlated. However, had the correlations exceed $-\frac{1}{4}$, this would have implied entanglement between the impurities, so that a measurement of each would affect the other, in violation of chirality.

Finally, in order to establish that despite the observed correlations, the local dynamics of the impurities are independent of the distance, we turn to the (retarded) spin-spin correlator and its corresponding spectral function $\mathcal{A}^S(\omega)$ [defined analogously to Eq. (7)]

$$\langle\langle S_m^+; S_{m'}^- \rangle\rangle_\omega = -i \int_{-\infty}^{\infty} \Theta(t) \langle [S_m^+(t), S_{m'}^-(0)] \rangle_{T \rightarrow 0} e^{i\omega t} dt, \quad (33a)$$

$$\mathcal{A}_{mm'}^S(\omega) = -\frac{1}{2\pi i} (\langle\langle S_m^+; S_{m'}^- \rangle\rangle_\omega - \langle\langle S_{m'}^+; S_m^- \rangle\rangle_\omega^*). \quad (33b)$$

In NRG we naturally obtain $\mathcal{A}^S(\omega)$ from the Lehman representation, and plot its diagonal elements

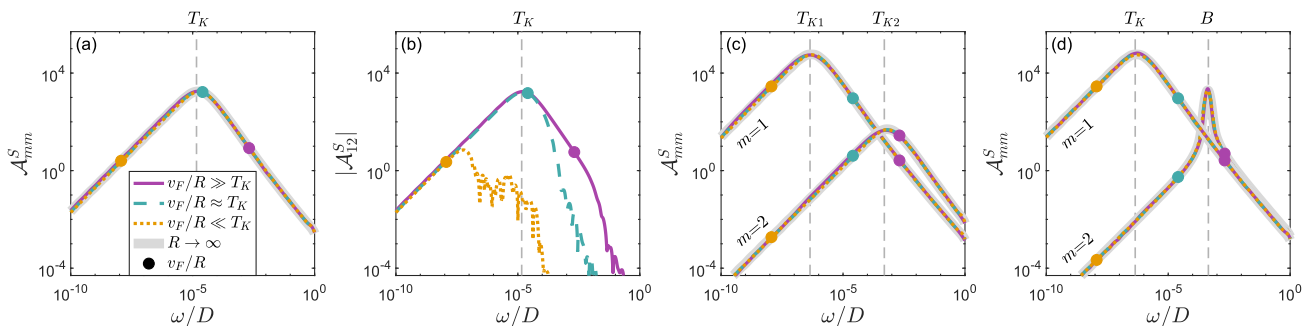


FIG. 6. Dynamic zero-temperature spin-spin correlations, for the same parameters as in Fig. 4 and averaged over four z shifts⁹: (a) Diagonal (local) $\mathcal{A}_{mm}^S(\omega) = -\frac{1}{\pi}\text{Im}\langle\langle S_m^+; S_m^- \rangle\rangle_\omega$, and (b) the envelope of the off-diagonal $|\mathcal{A}_{12}^S(\omega)| = |\mathcal{A}_{21}^{S*}(\omega)|$, spin spectral function, both calculated for equal couplings $J/D = 0.2$; [(c) and (d)] Response of the local spin spectral function to the breaking of impurity symmetry, either (c) by impurity-dependent couplings J_1 and J_2 , or (d) by taking equal coupling and introducing a magnetic field at the second impurity. The spectral function belonging to each impurity is labeled accordingly, and flipping between the couplings or magnetic fields returns the same result with flipped labels.

$-\frac{1}{\pi}\text{Im}\langle\langle S_m^+; S_m^- \rangle\rangle_\omega$ and (the envelope of its) off-diagonal elements in Figs. 6(a) and 6(b), respectively. Observe that for both impurities the local correlations [in Fig. 6(a)] coincide with the single-impurity (or $R \rightarrow \infty$, in shaded gray) results at all frequencies, displaying no signatures of the finite distance. The envelope of the off-diagonal elements [in Fig. 6(b)] coincides with the diagonal elements for $\omega < v_F/R$, as in the noninteracting case, while for higher frequencies it is noisy, which is unavoidable for a logarithmic discretization, and decays rapidly.

Due to chirality, we expect the retarded correlator to be upper-triangular,⁸ i.e., $\langle\langle S_2^+; S_1^- \rangle\rangle_\omega = 0$, implying no response at the first impurity to an event at the second impurity. Explicitly showing this requires numerically applying a Hilbert transform to $\mathcal{A}^S(\omega)$, which is infeasible due to the noise in the off-diagonal terms. However, we can still observe signatures of this chiral property directly in the spectral function by breaking the symmetry between the two impurities, i.e., by introducing impurity dependent couplings or magnetic fields, as shown in Figs. 6(c) and 6(d), respectively. For a chiral (i.e., upper-triangular) retarded correlator, the local (i.e., diagonal) elements of the corresponding spectral function should only depend on the local coupling and magnetic field [in analogy to hopping and chemical potential in the noninteracting case—see Eq. (6) and the following discussion]. This is indeed what we observe, conclusively demonstrating the effectiveness of our chiral NRG scheme in capturing chiral behavior, and showing that the local physics of each impurity are simply the single-impurity Kondo physics of separate impurities.

V. SUMMARY AND OUTLOOK

In this paper, we have introduced an extension of Wilson’s NRG for two impurities coupled to unidirectional channel(s) at a finite separation R . It is based on mapping each bath (channel) onto two coupled tight-binding Wilson chains, or a Wilson ladder, with the impurities coupled to one end of the ladder. As in a Wilson chain, the energy scales along the Wilson ladder decay exponentially with the distance from the impurities. We find that in the vicinity of the impurities, corresponding to high energies or short wavelengths with respect to R , the two chains are only weakly coupled. On the other hand, at low energies or long wavelengths with respect to the interimpurity separation, we effectively get a single Wilson chain (with small next-next nearest neighbor corrections), which corresponds to the impurities being coupled to the bath at *almost* the same point. However, it should be stressed that the impurities are never exactly at the same point, and we always retain the notion of some finite separation, which ensures the unidirectionality of the channel. In this work, we restricted ourselves to two impurities, but in principle the same procedure should apply to an arbitrary number of impurities, resulting in a Wilson chain for each impurity, which is then coupled to the other chains. We have also restricted ourselves to a featureless bath density of states, corresponding to a linear chiral dispersion, but the presented method can be applied to an arbitrary chiral or helical dispersion.

We demonstrated the power of the mapping to the Wilson ladder on a spinless noninteracting (analytically

⁸ This chirality of the retarded correlators, i.e., upper-triangular structure, also in the presence of interactions, could be shown order-by-order in Keldysh perturbation theory, in a similar way to showing that the retardedness is preserved [67].

⁹ The discretization can impair chirality, leaving signatures on the spectral function for individual z shifts. These are typically

washed out after z -averaging or by taking smaller Λ , as these are better approximations for the (chiral) continuum limit. The smallest R (in purple) turns out to be most sensitive to this, and thus require cranking up the NRG parameters: In Fig. 6(d), taking $\Lambda = 2.5$ (with 7000 kept multiplets) suffices, while in Fig. 6(c), we also linearly extrapolate to the continuum limit in $\Lambda = 3, 2 \rightarrow 1$ (with 8000 kept multiplets for $\Lambda = 2$).

solvable) system consisting of two resonant levels coupled to a single unidirectional channel. We showed that local impurity properties and thermodynamic quantities are indifferent to the distance between the impurities, and are thus equal to those of two infinitely spaced, i.e., independent, impurity models. This is a key signature of chirality. We also successfully captured interimpurity correlations at low energies, while at high energies, for which the correlations are highly oscillatory (and decay), we only captured noise (albeit around zero). Introducing spin and interactions, we applied the method to two impurities coupled antiferromagnetically to a single spinful chiral channel. Similarly to the noninteracting test case, we found that all considered local and thermodynamic quantities are independent of the interimpurity distance, and thus follow the universal curves (of two copies) of the single-impurity Kondo effect. Again, interimpurity correlations were successfully captured at low energies while oscillatory around zero at high energies. The key observation is that although such *static* correlations exist, they are not due to effective (e.g., RKKY) interactions between the impurities, which are forbidden due to chirality. Hence, interimpurity response functions (*retarded* correlations) remain chiral, and the system locally behaves like two separate single-impurity problems, regardless of the *finite* distance between the two impurities.

Our goal in this paper was to demonstrate how NRG can be applied to unidirectional channels. Once we have established this, there are many prospective applications. One interesting direction is to look at helical systems, even in the single channel case. Such systems were explored analytically in different limits [25–28], but the presented method enables a quantitative study of the transition between an RKKY phase and a Kondo-screened phase. Another direction relates to our initial motivation for this work—studying multi-impurity chiral multichannel Kondo systems. In Ref. [39], we studied such a system, demonstrating the emergence of decoupled non-Abelian anyons, for which the fusion channel could be measured by looking at interimpurity spin correlations. There we relied on arguments for interimpurity distance independence in order to simplify the problem by taking the limit $R \rightarrow 0^+$. In this work, we support these arguments with numerical results for a single-channel model, but also demonstrate that the distance does enter in nonuniversal quantities such as zero-temperature value of the interimpurity correlations. Thus, it would be interesting to study the correlations in the multichannel case with the help of the Wilson ladder, in order to discern between the nonuniversal distant-dependent properties, and the universal properties related to the measurement of the fusion channel.

Note added: Recently, we were made aware of a related work by Ferrer *et al.* [68], dealing with multiple impurities on a helical edge, and agreed on a synchronized preprint submission.

Acknowledgments: We would like to thank J. von Delft, A. Weichselbaum, S.-S. Lee, and N. Andrei for

fruitful discussions. Numerical simulations were performed using the QSPACE tensor-network library and accompanying code [60, 63, 64, 69]. Support from the Rutgers Tel-Aviv university joined fund is gratefully acknowledged. E.S. was further supported by the Synergy funding for Project No. 941541, ARO (W911NF-20-1-0013), the US-Israel Binational Science Foundation (BSF) Grant No. 2016255, and the Israel Science Foundation (ISF) Grant No. 154/19. M.G. was supported by the ISF and the Directorate for Defense Research and Development (DDR&D) Grant No. 3427/21 and by the BSF Grant No. 2020072.

Appendix A: Discretization Following Ref. [50]

In this appendix, we will derive explicit expressions for the coefficient matrices \mathbf{V}_n and \mathcal{E}_n in the spirit of the discretization procedure by Campo and Oliveira [50]. The obtained expressions will differ from those in Sec. II A by a unitary rotation of each set of modes \mathbf{c}_n [see Eq. (A10)]. At the end of the appendix, we also compare with the notation of Ref. [59].

We start this derivation by Fourier transforming to k -space, in which the bath Hamiltonian is diagonal, and there we introduce the high-energy cutoff $D = v_F k_{\max}$, where, as mentioned, for a chiral system k_{\max} should not be associated with the Fermi wavevector k_F or an underlying lattice spacing:

$$H_{\text{bath}} = \int_{-k_{\max}}^{k_{\max}} \frac{dk}{2\pi} v_F k c_k^\dagger c_k, \quad (\text{A1a})$$

$$\psi(x) = \int_{-k_{\max}}^{k_{\max}} \frac{dk}{2\pi} e^{ikx} c_k \equiv \sqrt{\frac{k_{\max}}{\pi}} \tilde{\psi}(x). \quad (\text{A1b})$$

The fermionic operators c_k and $\tilde{\psi}(x)$ satisfy $\{c_k, c_{k'}^\dagger\} = 2\pi\delta(k-k')$ and $\{\tilde{\psi}(x), \tilde{\psi}^\dagger(x)\} = 1$, respectively. Note that the cutoff impairs the orthogonality relations of the field operators at the impurities $\{\tilde{\psi}(-R/2), \tilde{\psi}^\dagger(+R/2)\} = \text{sinc}(k_{\max}R)$, but this can be amended by choosing the cutoff to be commensurate with R as in Eq. (13).

We then write the normalized combinations of bath modes to which the impurity modes d_+ and d_- [defined in Eq. (9)] couple:

$$f_{0+} = \int_{-k_{\max}}^{k_{\max}} \frac{dk}{2\pi} \sqrt{\frac{2\pi}{k_{\max}}} \cos(kR/2) c_k, \quad (\text{A2a})$$

$$f_{0-} = \int_{-k_{\max}}^{k_{\max}} \frac{dk}{2\pi} \sqrt{\frac{2\pi}{k_{\max}}} \sin(kR/2) c_k. \quad (\text{A2b})$$

Switching to 2-vector notation, we can write the coupling Hamiltonian as

$$H_{\text{coupling}} = \mathbf{d}^\dagger \mathbf{T}_0 \mathbf{f}_0 + \text{H.c.}, \quad (\text{A3a})$$

$$\mathbf{T}_0 = \begin{pmatrix} t_0 & 0 \\ 0 & t_0 \end{pmatrix}, \quad t_0 = \sqrt{\frac{k_{\max}}{\pi}} \tilde{t}_0 = \sqrt{\frac{2D\Gamma}{\pi}}. \quad (\text{A3b})$$

Note that taking a cutoff which is not commensurate with R only affects the normalization of the even-odd modes \mathbf{f}_0 , but by construction they are still orthogonal. Thus, introducing normalization constants $\mathcal{N}_\pm = 1 \pm \text{sinc}(k_{\max}R)$, we get

$$\mathbf{f}_0 \rightarrow \begin{pmatrix} \sqrt{\mathcal{N}_+} & 0 \\ 0 & \sqrt{\mathcal{N}_-} \end{pmatrix}^{-1} \mathbf{f}_0, \quad \mathbf{T}_0 \rightarrow \begin{pmatrix} \sqrt{\mathcal{N}_+} & 0 \\ 0 & \sqrt{\mathcal{N}_-} \end{pmatrix} \mathbf{T}_0, \quad (\text{A4})$$

which leaves the product $\mathbf{T}_0 \mathbf{f}_0$ unchanged. As this does not affect the rest of the discretization procedure in any way, i.e., the expressions for \mathbf{V}_n and \mathcal{E}_n remain unchanged, and the modified \mathbf{T}_0 is automatically obtained from the numerical tridiagonalization, we can forget about it for the rest of the derivation.

Exploiting particle-hole symmetry [see Eq. (3a), which translates to invariance under $c_k \rightarrow c_{-k}^\dagger, d_m \rightarrow -d_m^\dagger$], we can restrict the discretization procedure to positive k , and obtain the negative k coefficients by symmetry. We redefine the discretization gridpoints to k -space (focusing on positive k and n)

$$k_1^z = k_{\max}, \quad k_{n>1}^z = k_{\max} \Lambda^{2-n-z}, \quad (\text{A5})$$

and the intervals $I_n^z = [k_{n+1}^z, k_n^z]$, denoting their width and midpoints

$$\Delta k_n^z \equiv k_n^z - k_{n+1}^z, \quad \bar{k}_n^z \equiv \frac{k_n^z + k_{n+1}^z}{2}. \quad (\text{A6})$$

For conciseness, we now drop the z index, but it is implied whenever n appears.

In each interval, each impurity is coupled only to a single mode, defined by limiting the support of the integrals in Eq. (A2) to I_n . These modes are generally not orthogonal with respect to each other, but we can always choose linear combinations of the two which are orthonormal, for example:

$$c_{n\pm} = \int_{I_n} \frac{dk}{2\pi} \varphi_{n\pm}(k) c_k, \quad (\text{A7a})$$

$$\varphi_{n+}(k) = \sqrt{\frac{4\pi}{\Delta k_n}} \frac{\cos[(k - \bar{k}_n)R/2]}{\sqrt{1 + \text{sinc}(\Delta k_n R/2)}}, \quad (\text{A7b})$$

$$\varphi_{n-}(k) = \sqrt{\frac{4\pi}{\Delta k_n}} \frac{\sin[(k - \bar{k}_n)R/2]}{\sqrt{1 - \text{sinc}(\Delta k_n R/2)}}, \quad (\text{A7c})$$

with their coupling to the impurities given by the product of a rotation matrix and a rescaling matrix

$$\begin{aligned} \mathbf{V}_n &= t_0 \sqrt{\frac{\Delta k_n}{2k_{\max}}} \mathbf{R}_n \mathbf{S}_n, \\ \mathbf{R}_n &= \begin{pmatrix} \cos(\bar{k}_n R/2) & -\sin(\bar{k}_n R/2) \\ +\sin(\bar{k}_n R/2) & \cos(\bar{k}_n R/2) \end{pmatrix}, \\ \mathbf{S}_n &= \begin{pmatrix} \sqrt{1 + \text{sinc}(\frac{\Delta k_n R}{2})} & 0 \\ 0 & \sqrt{1 - \text{sinc}(\frac{\Delta k_n R}{2})} \end{pmatrix}. \end{aligned} \quad (\text{A8})$$

Observe that the chosen \mathbf{c}_n are PT symmetric, which, as expected, results in real \mathbf{V}_n . The hybridization function of Eq. (10) is given by

$$\Gamma(\omega) = \Gamma \frac{\Delta k_n}{2\pi} \mathbf{R}_n \mathbf{S}_n \begin{pmatrix} \varphi_{n+}^2(k) & \varphi_{n+}(k)\varphi_{n-}(k) \\ \varphi_{n+}(k)\varphi_{n-}(k) & \varphi_{n-}^2(k) \end{pmatrix} \mathbf{S}_n \mathbf{R}_n^\dagger, \quad (\text{A9})$$

where n and k are chosen such that $k = \omega/v_F \in I_n$. It is then evident that the coefficient matrices and modes $\mathbf{c}_n \equiv \begin{pmatrix} c_{n+} \\ c_{n-} \end{pmatrix}$ defined in this appendix differ from those in Sec. II A by the rotation \mathbf{R}_n

$$\mathbf{c}_n^{\text{Sec.II}} = \mathbf{R}_n \mathbf{c}_n, \quad \mathbf{V}_n^{\text{Sec.II}} = \mathbf{V}_n \mathbf{R}_n^\dagger, \quad \mathcal{E}_n^{\text{Sec.II}} = \mathbf{R}_n \mathcal{E}_n \mathbf{R}_n^\dagger. \quad (\text{A10})$$

$\mathbf{V}_n \mathbf{c}_n$ and $\mathbf{c}_n^\dagger \mathcal{E}_n \mathbf{c}_n$, however, are unaffected, and Eq. (19) still relates the negative n coefficient matrices to those with positive n . With this in hand, one can show that the expressions below in Eqs. (A14) and (A21) lead to Eqs. (17) and (18), respectively.

Following in the steps of Ref. [50], we start by extending the traditional *naive* discretization scheme (dating back to Wilson) to the chiral two-impurity scenario. In each interval I_n , we define a real orthonormal basis of functions $\varphi_{n\xi}(k)$ (to be specified later on), which satisfy the orthogonality condition

$$\int_{I_n} \frac{dk}{2\pi} \varphi_{n\xi}(k) \varphi_{n\xi'}(k) = \delta_{\xi\xi'}. \quad (\text{A11})$$

We then use these functions to define a canonical basis of fermionic modes

$$c_{n\xi} = \int_{I_n} \frac{dk}{2\pi} \varphi_{n\xi}(k) c_k \quad (\text{A12a})$$

$$c_k = \sum_{\xi} \varphi_{n\xi}(k) c_{n\xi}; \quad k \in I_n \quad (\text{A12b})$$

Substituting this into the bath Hamiltonian in Eq. (A1a), we obtain

$$\begin{aligned} H_{\text{bath}} &= \sum_{n=\pm 1}^{\pm N} \int_{I_n} \frac{dk}{2\pi} v_F k c_k^\dagger c_k \\ &= \sum_{n=\pm 1}^{\pm N} \sum_{\xi\xi'} \left[\int_{I_n} \frac{dk}{2\pi} v_F k \varphi_{n\xi}(k) \varphi_{n\xi'}(k) \right] c_{n\xi}^\dagger c_{n\xi'}. \end{aligned} \quad (\text{A13})$$

We now wish to choose two specific modes (in each interval), c_{n1} and c_{n2} , which span the space of modes coupled to the impurities, i.e., that spanned by c_{n+} and c_{n-} . We find that $\varphi_{n1}(k) \equiv \varphi_{n+}(k)$ and $\varphi_{n2}(k) \equiv \varphi_{n-}(k)$ [specified in Eq. (A7)] already satisfy Eq. (A11), and so $\mathbf{c}_n = \begin{pmatrix} c_{n+} \\ c_{n-} \end{pmatrix} = \begin{pmatrix} c_{n1} \\ c_{n2} \end{pmatrix}$. Thus, projecting out all other modes (which are never constructed explicitly) leaves us with the coefficient matrix

$$\mathcal{E}_n^{\text{naive}} = \int_{I_n} \frac{dk}{2\pi} v_F k \begin{pmatrix} \varphi_{n+}^2(k) & \varphi_{n+}(k)\varphi_{n-}(k) \\ \varphi_{n+}(k)\varphi_{n-}(k) & \varphi_{n-}^2(k) \end{pmatrix}. \quad (\text{A14})$$

We can then solve the integrals explicitly and obtain

$$\mathcal{E}_n^{\text{naive}} = v_F \bar{k}_n \begin{pmatrix} 1 & \alpha_n \\ \alpha_n & 1 \end{pmatrix}, \quad (\text{A15a})$$

$$\alpha_n = \frac{\text{sinc}(\Delta k_n R/2) - \cos(\Delta k_n R/2)}{\bar{k}_n R \sqrt{1 - \text{sinc}^2(\Delta k_n R/2)}}. \quad (\text{A15b})$$

Observe that the diagonal terms are simply the interval midpoints, as one would indeed expect from the naive scheme. At short wavelengths (high energies) the off diagonal terms are negligible (of order v_F/R), corresponding to the picture of two decoupled chains, while for long wavelengths they are of order of (but smaller than) the diagonal terms (for any finite Λ), and one can no longer consider the chiral channel as two separate baths.

We now turn to extend the *improved* discretization scheme of Ref. [50] to the chiral two-impurity scenario. We start by defining a real set of functions $\tilde{\varphi}_{n\xi}(k)$ (to be specified later on), which satisfy a weighted orthogonality condition, but are still normalized with respect to the unweighted inner product

$$\int_{I_n} \frac{dk}{2\pi} \frac{1}{k} \tilde{\varphi}_{n\xi}(k) \tilde{\varphi}_{n\xi'}(k) = \frac{\delta_{\xi\xi'}}{\mathcal{K}_{n\xi}}, \quad (\text{A16a})$$

$$\int_{I_n} \frac{dk}{2\pi} \tilde{\varphi}_{n\xi}(k) \tilde{\varphi}_{n\xi'}(k) = 1, \quad (\text{A16b})$$

where \mathcal{K}_n is a diagonal matrix (with elements $\mathcal{K}_{n\xi}$) chosen such that Eq. (A16b) is satisfied. We use these to define a nonorthogonal (but normalized) basis of modes

$$\tilde{c}_{n\xi} = \int_{I_n} \frac{dk}{2\pi} \tilde{\varphi}_{n\xi}(k) c_k, \quad (\text{A17a})$$

$$c_k = \sum_{\xi} \frac{\mathcal{K}_{n\xi}}{k} \tilde{\varphi}_{n\xi}(k) \tilde{c}_{n\xi}; \quad k \in I_n. \quad (\text{A17b})$$

As before, we substitute c_k into the bath Hamiltonian, and find that in our nonorthogonal basis, H_{bath} is diagonal

$$H_{\text{bath}} = \sum_{n=\pm 1}^{\pm N} \sum_{\xi} v_F \mathcal{K}_{n\xi} \tilde{c}_{n\xi}^{\dagger} \tilde{c}_{n\xi}. \quad (\text{A18})$$

Again we wish to keep only two specific modes, \tilde{c}_{n1} and \tilde{c}_{n2} , which span the space of modes coupled to the impurities. We are thus looking for modes related to our original $\mathbf{c}_n = (c_{n1}, c_{n2})$ by an orthogonal transformation \mathbf{O}_n :

$$\begin{pmatrix} \tilde{c}_{n1} \\ \tilde{c}_{n2} \end{pmatrix} = \mathbf{O}_n \begin{pmatrix} c_{n1} \\ c_{n2} \end{pmatrix}, \quad \begin{pmatrix} \tilde{\varphi}_{n1}(k) \\ \tilde{\varphi}_{n2}(k) \end{pmatrix} = \mathbf{O}_n \begin{pmatrix} \varphi_{n1}(k) \\ \varphi_{n2}(k) \end{pmatrix}, \quad (\text{A19})$$

such that $\tilde{\varphi}_{n1}(k)$ and $\tilde{\varphi}_{n2}(k)$ satisfy Eq. (A16), with $\varphi_{n1}(k) = \varphi_{n+}(k)$ and $\varphi_{n2}(k) = \varphi_{n-}(k)$ as specified above. We find \mathbf{O}_n by diagonalizing the symmetric matrix

$$\mathbf{K}_n^{-1} = \int_{I_n} \frac{dk}{2\pi} \frac{1}{k} \begin{pmatrix} \varphi_{n1}^2(k) & \varphi_{n1}(k)\varphi_{n2}(k) \\ \varphi_{n1}(k)\varphi_{n2}(k) & \varphi_{n2}^2(k) \end{pmatrix}, \quad (\text{A20a})$$

$$\mathcal{K}_n^{-1} = \mathbf{O}_n \mathbf{K}_n^{-1} \mathbf{O}_n^{\dagger} = \begin{pmatrix} \mathcal{K}_{n1} & 0 \\ 0 & \mathcal{K}_{n2} \end{pmatrix}^{-1}. \quad (\text{A20b})$$

We can now discard all modes in Eq. (A18) except $\tilde{c}_{n1}, \tilde{c}_{n2}$, and use \mathbf{O}_n to rewrite H_{bath} in terms of c_{n1}, c_{n2} , to get $\mathcal{E}_n^{\text{CO}} = v_F \mathbf{K}_n$ (switching notation back to $\{+, -\} = \{1, 2\}$):

$$\mathcal{E}_n^{\text{CO}} = \left[\int_{I_n} \frac{dk}{2\pi} \frac{1}{v_F k} \begin{pmatrix} \varphi_{n+}^2(k) & \varphi_{n+}(k)\varphi_{n-}(k) \\ \varphi_{n+}(k)\varphi_{n-}(k) & \varphi_{n-}^2(k) \end{pmatrix} \right]^{-1}. \quad (\text{A21})$$

Note that in practice we only calculate \mathbf{K}_n , and never construct \mathbf{O}_n and \mathcal{K}_n .

Solving the integral for \mathbf{K}_n^{-1} , we obtain

$$[\mathbf{K}_n^{-1}]_{\pm\pm} = \frac{1}{\mathcal{N}_{n\pm}} [\log r_n \pm C_n \Delta \mathcal{C}_n \pm S_n \Delta \mathcal{S}_n], \quad (\text{A22a})$$

$$[\mathbf{K}_n^{-1}]_{\pm\mp} = \frac{1}{\sqrt{\mathcal{N}_{n+}\mathcal{N}_{n-}}} [C_n \Delta \mathcal{S}_n - S_n \Delta \mathcal{C}_n], \quad (\text{A22b})$$

$$\mathcal{N}_{n\pm} = \Delta k_n (1 \pm \text{sinc}(\Delta k_n R/2)), \quad (\text{A22c})$$

$$r_n = k_n/k_{n+1}, \quad C_n = \cos(\bar{k}_n R), \quad S_n = \sin(\bar{k}_n R), \quad (\text{A22d})$$

$$\Delta \mathcal{C}_n = \int_{k_{n+1}R}^{k_n R} \frac{\cos(x)}{x} dx, \quad \Delta \mathcal{S}_n = \int_{k_{n+1}R}^{k_n R} \frac{\sin(x)}{x} dx. \quad (\text{A22e})$$

Observe that for short wavelengths (high energies) the off diagonal terms $[\mathbf{K}_n^{-1}]_{\pm\mp}$ vanish, corresponding to two decoupled baths, while the diagonal terms approach $[\mathbf{K}_n^{-1}]_{\pm\pm} \rightarrow \frac{\log k_n - \log k_{n+1}}{k_n - k_{n+1}}$, so that inverting we get the discrete energies $\mathcal{E}_{n\pm\pm} \rightarrow \frac{1-\Lambda^{-1}}{\log \Lambda} D \Lambda^{2-n-z}$ expected from the scheme of Ref. [50] [see Eq. (46) therein]. In the opposite limit of long wavelengths, the chiral channel can no longer be considered as two separate baths, and indeed all elements of \mathbf{K}_n^{-1} survive.

As a final step, we would like to compare with notation used in Ref. [59] to describe the discretization scheme of Ref. [50]. We thus first write the local density of states for the modes \mathbf{f}_0 coupled to the impurities

$$\rho(\omega) = \pi \mathbf{T}_0^{-1} \mathbf{\Gamma}(\omega) \mathbf{T}_0^{-1}, \quad [\mathbf{T}_0]^2 = \frac{1}{\pi} \int_{-D}^D \mathbf{\Gamma}(\omega) d\omega, \quad (\text{A23})$$

so that $\int_{-D}^D \rho(\omega) = \mathbf{1}$. Then Eq. (30) in Ref. [59] takes the form

$$\mathbf{f}_0 = \sum_n \left[\int_{I_n} \rho(\omega) d\omega \right]^{\frac{1}{2}} \mathbf{c}_n, \quad (\text{A24})$$

where taking the square root is well defined because $\rho(\omega)$ is positive. We then rewrite Eqs. (17) and (18) as

$$\mathcal{E}_n^{\text{naive}} = \left[\int_{I_n} \rho(\omega) d\omega \right]^{-\frac{1}{2}} \left[\int_{I_n} \rho(\omega) \omega d\omega \right] \left[\int_{I_n} \rho(\omega) d\omega \right]^{-\frac{1}{2}}, \quad (\text{A25})$$

$$\mathcal{E}_n^{\text{CO}} = \left[\int_{I_n} \rho(\omega) d\omega \right]^{\frac{1}{2}} \left[\int_{I_n} \rho(\omega) \frac{d\omega}{\omega} \right]^{-1} \left[\int_{I_n} \rho(\omega) d\omega \right]^{\frac{1}{2}}, \quad (\text{A26})$$

which is the matrix generalization of Eqs. (33) and (32) in Ref. [59], respectively.

Appendix B: Exploiting Symmetries

In this appendix we discuss technical aspects in the exploitation of symmetries as part of our chiral NRG scheme. We focus on the $\text{SU}(2)_{\text{charge}} \otimes \text{SU}(2)_{\text{spin}}$ symmetric case, but the discussion below also applies (with some simplifications) to the $\text{U}(1)_{\text{charge}} \otimes \text{SU}(2)_{\text{spin}}$ symmetric case, while for the $\text{U}(1)_{\text{charge}} \otimes \text{U}(1)_{\text{spin}}$ symmetric case it becomes trivial (and so irrelevant).

We start with a brief overview of the way symmetry-respecting tensors are formulated in the QSPACE library, with the full details given in Ref. [63]. Similarly to the decomposition in the Wigner-Eckart theorem [70], for a general non-Abelian symmetry, each tensor can be decomposed into an outer product of (generalized) reduced matrix elements, and (generalized) Clebsch-Gordan coefficients. We write (and track) only the tensors describing the reduced matrix elements, which limits the operators we can access (to those respecting the symmetry, which should be all we need). In the case of $SU(2)_{\text{charge}} \otimes SU(2)_{\text{spin}}$, these are given by (see Appendix A.9 of Ref. [63])

$$\mathbf{F}_m = \begin{pmatrix} (-1)^m f_{m\uparrow}^\dagger \\ f_{m\downarrow} \\ (-1)^m f_{m\downarrow}^\dagger \\ -f_{m\uparrow} \end{pmatrix}, \quad \mathbf{S}_m = \begin{pmatrix} -\frac{1}{\sqrt{2}} S_m^+ \\ S_m^z \\ +\frac{1}{\sqrt{2}} S_m^- \end{pmatrix}, \quad \mathbf{C}_m = \begin{pmatrix} -\frac{1}{\sqrt{2}} C_m^+ \\ C_m^z \\ +\frac{1}{\sqrt{2}} C_m^- \end{pmatrix}, \quad (\text{B1})$$

where $f_{m\sigma}$ are fermionic operators at site m with spin σ , and S_i (C_i) are the spin (charge) $SU(2)$ operators. We then use these operators in order to construct operators which are scalars with respect to the symmetry, with the Hamiltonian being a sum of such scalars.

The site index m bipartitions the sites according to its parity (and can, but does not have to, coincide with the fermionic order for the Jordan-Wigner string). The structure of Eq. (B1) then allows only purely real (imaginary) hopping terms if m and m' have different (same) parity

$$m+m' \text{ odd} : \quad \mathbf{F}_m^\dagger \mathbf{F}_{m'} = \sum_{\sigma} (f_{m\sigma}^\dagger f_{m'\sigma} + f_{m'\sigma}^\dagger f_{m\sigma}), \quad (\text{B2a})$$

$$m+m' \text{ even} : \quad i\mathbf{F}_m^\dagger \mathbf{F}_{m'} = i \sum_{\sigma} (f_{m\sigma}^\dagger f_{m'\sigma} - f_{m'\sigma}^\dagger f_{m\sigma}). \quad (\text{B2b})$$

We recall that the Wilson ladder (in the even-odd PT-symmetric basis) has only real hopping amplitudes, and indeed, by choosing m to snake along the ladder ($d_+ \rightarrow d_- \rightarrow f_0 \rightarrow f_0 \rightarrow f_1 \rightarrow f_1 \rightarrow f_2 \rightarrow \dots$) all hopping terms are between sites of opposite parity, as dictated by symmetry. If we return to the real-space basis, as discussed at the end of Sec. II B, we will have both purely imaginary and purely real terms (but no complex terms), and can choose a different ordering for m such that all terms adhere to Eq. (B2).

We now turn to the interaction terms, which can indeed be constructed from the operators in Eq. (B1), both for the Kondo model [Eq. (31)]: $\mathbf{S}_m^\dagger \mathbf{S}_{m'} = \tilde{S}_m \cdot \tilde{S}_{m'}$, and for the Anderson model [Eq. (30), after taking $\varepsilon_d = -U/2$]

$$\begin{aligned} \frac{4}{3} \mathbf{C}_m^\dagger \mathbf{C}_m &= (n_{m\uparrow} + n_{m\downarrow} - 1)^2 & (\text{B3}) \\ &= 2n_{m\uparrow}n_{m\downarrow} - (n_{m\uparrow} + n_{m\downarrow}) + 1 \\ &= 1 - (n_{m\uparrow} - n_{m\downarrow})^2 = 1 - \frac{4}{3} \mathbf{S}_m^\dagger \mathbf{S}_m. \end{aligned}$$

These (real) terms are defined in the real-space basis, whereas the Wilson ladder is real in the even-odd PT-symmetric basis. If we transform the entire (or part of the) Wilson ladder back to real-space, we will generate

imaginary terms. However, as the interaction terms are invariant under a PT transformation, if we write them in terms of PT-symmetric fermionic (or spin) operators, we are guaranteed to have real coefficients. Thus, the full Hamiltonian is purely real, and we can restrict the numerical iterative diagonalization to real (double precision) arithmetic, which significantly reduces the computational cost. The transforming of the interaction terms to the PT-symmetric basis is derived in the remainder of this appendix.

Consider two fermionic sites $m \in \{1, 2\}$ with spinful operators $f_{m\sigma}$, which correspond e.g., to the two impurity sites \mathbf{d} or the first two ladder sites \mathbf{f}_0 . We define a basis transformation with respect to the site index

$$\tilde{f}_{m\sigma} = \sum_{m'} u_{mm'} f_{m'\sigma}, \quad (\text{B4})$$

where u is a 2×2 unitary matrix, e.g., $u = \frac{1}{\sqrt{2}} \begin{pmatrix} 1 & -1 \\ i & i \end{pmatrix}$ for the transformation to PT-symmetric modes in Eqs. (9) and (A2). The corresponding operators $\mathbf{F}_1, \mathbf{F}_2$ trivially transform accordingly, so that we can immediately write them in terms of the operators $\tilde{\mathbf{F}}_1, \tilde{\mathbf{F}}_2$, and vice versa. However, it is not *a priori* clear how the $SU(2)$ operators, e.g., $\mathbf{S}_1, \mathbf{S}_2$, transform, and how to write them if we only have access to $\tilde{\mathbf{S}}_1, \tilde{\mathbf{S}}_2$. Generically we would like to relate operators which are quadratic in $f_{m\sigma}$ and diagonal with respect to m in the original basis, i.e., can be written as

$$O_m = \sum_{\sigma\sigma'} O_{\sigma\sigma'} f_{m\sigma}^\dagger f_{m\sigma'}, \quad (\text{B5})$$

to those which are quadratic in $\tilde{f}_{m\sigma}$ and diagonal with respect to m in the new basis,

$$\tilde{O}_m = \sum_{\sigma\sigma'} O_{\sigma\sigma'} \tilde{f}_{m\sigma}^\dagger \tilde{f}_{m\sigma'} = \sum_{\sigma\sigma'} \sum_{l'l'} O_{\sigma\sigma'} f_{l\sigma}^\dagger u_{lm}^\dagger u_{ml'} f_{l'\sigma'}. \quad (\text{B6})$$

If we exploit only Abelian symmetries, we have access to the individual fermionic operators, and can write the individual quadratic $f_{l\sigma}^\dagger f_{l'\sigma'}$ terms, but for non-Abelian symmetries we only have access to specific combinations, e.g., only $\mathbf{F}_1^\dagger \mathbf{F}_2$ (and $\tilde{\mathbf{F}}_1^\dagger \tilde{\mathbf{F}}_2$) in the $SU(2)_{\text{charge}} \otimes SU(2)_{\text{spin}}$ case. We would thus like to directly express O_m in terms of \tilde{O}_m , using only the allowed combinations.

In order to do so, we first observe that if we write each operator $f_{m\sigma}$ as a matrix acting on the two-site Hilbert space, then we have a unitary matrix U acting on the same space such that

$$\tilde{f}_{m\sigma} = U^\dagger f_{m\sigma} U, \quad U \equiv \exp\left(\sum_{mm'\sigma} [\log u]_{mm'} f_{m\sigma}^\dagger f_{m'\sigma}\right), \quad (\text{B7})$$

where $\log u$ is the matrix logarithm of the transformation matrix u . Substituting this into into Eq. (B6) we immediately get

$$\tilde{O}_m = \sum_{\sigma\sigma'} O_{\sigma\sigma'} U^\dagger f_{m\sigma}^\dagger U U^\dagger f_{m\sigma'} U = U^\dagger O_m U. \quad (\text{B8})$$

For completeness we prove Eq. (B7). It is convenient to first diagonalize u , and write U in the basis defined by this diagonalization

$$u_{mm'} = \sum_l s_{ml}^\dagger e^{i\phi_l} s_{lm'}, \quad \tilde{f}_{m\sigma} = \sum_{m'} s_{mm'} f_{m'\sigma}, \quad (\text{B9a})$$

$$U = \exp\left(i \sum_{lm} s_{ml}^\dagger \phi_l s_{lm'} f_{m\sigma}^\dagger f_{m'\sigma}\right) = \exp\left(i \sum_{l\sigma} \phi_l \tilde{f}_{l\sigma}^\dagger \tilde{f}_{l\sigma}\right), \quad (\text{B9b})$$

with s a unitary matrix and ϕ_l a phase. Substituting this into the r.h.s. of Eq. (B7), we arrive at its l.h.s.,

$$\begin{aligned} U^\dagger f_{m\alpha} U &= \exp\left(-i \sum_{\alpha\alpha'} \phi_\alpha \tilde{f}_{\alpha\alpha'}^\dagger \tilde{f}_{\alpha\alpha'}\right) \\ &\cdot \left(\sum_{lm'} s_{ml}^\dagger s_{lm'} f_{m'\sigma}\right) \cdot \exp\left(\sum_{b\beta} i \phi_b \tilde{f}_{b\beta}^\dagger \tilde{f}_{b\beta}\right) \\ &= \sum_l s_{ml}^\dagger e^{-i\phi_l} \tilde{f}_{l\sigma}^\dagger \tilde{f}_{l\sigma} \tilde{f}_{l\sigma} e^{i\phi_l} \tilde{f}_{l\sigma} \\ &= \sum_{lm'} s_{ml}^\dagger e^{i\phi_l} s_{lm'} f_{m'\sigma} = \sum_{m'} u_{mm'} f_{m'\sigma} = \tilde{f}_{m\sigma}. \end{aligned} \quad (\text{B10})$$

We have thus reduced the question to whether for a given u , we can write U as in Eq. (B7) using only operators respected by the symmetry, i.e., can we write $\log u = i\alpha\sigma_x$, and then $U = \exp(i\alpha\mathbf{F}_1^\dagger\mathbf{F}_2)$. This is generically not possible, and in particular not for $u = \frac{1}{\sqrt{2}} \begin{pmatrix} 1 & 1 \\ i & -i \end{pmatrix}$. However, we are only interested in finding a U which transforms quadratic operators, and do not require it to correctly transform the individual fermionic operators. As O_m and \tilde{O}_m are indifferent to phases $f_{m\sigma} \rightarrow e^{i\theta_m} f_{m\sigma}$ and $\tilde{f}_{m\sigma} \rightarrow e^{i\tilde{\theta}_m} \tilde{f}_{m\sigma}$, if we can find

$$v = \begin{pmatrix} e^{i\tilde{\theta}_1} & 0 \\ 0 & e^{i\tilde{\theta}_2} \end{pmatrix} u \begin{pmatrix} e^{-i\theta_1} & 0 \\ 0 & e^{-i\theta_2} \end{pmatrix} \text{ s.t. } \log v = i\alpha\sigma_x, \quad (\text{B11})$$

then $U = \exp(i\alpha\mathbf{F}_1^\dagger\mathbf{F}_2)$ will satisfy Eq. (B8) [although not Eq. (B7)]. Indeed, in our specific case, we find such a v :

$$v = \frac{1}{\sqrt{2}} \begin{pmatrix} 1 & i \\ i & 1 \end{pmatrix} = \frac{1}{\sqrt{2}} \begin{pmatrix} 1 & 1 \\ i & -i \end{pmatrix} \begin{pmatrix} 1 & 0 \\ 0 & i \end{pmatrix}, \quad \log v = i\frac{\pi}{4}\sigma_x. \quad (\text{B12})$$

For the Anderson model, we then transform the operators \mathbf{S}_+ , \mathbf{S}_- of the even-odd impurities to those in real-space $\mathbf{S}_1, \mathbf{S}_2$ and use them to write the interaction term.

For the Kondo model, we similarly use the even-odd basis spin operators at the first ladder sites $\mathbf{s}_{0\pm}$ in order to write those in real space $\mathbf{s}(\pm R/2)$. We also define \mathbf{S}_\pm as the even-odd basis impurity operators, and these transform trivially to real-space $(\mathbf{S}_\pm^1) = u^\dagger (\mathbf{S}_\pm^+)$, so that we can write the Kondo term. Assuming equal Coulomb or Kondo interactions at both impurities, we thus arrive at a real interaction Hamiltonian.

Appendix C: Single-Particle Calculations

For the noninteracting calculations of the discrete model, we write the full single-particle Hamiltonian as a matrix H and the bath single-particle Hamiltonian as a matrix H_0 (which is the same as H , excluding the impurity rows and columns). We then diagonalize $H = UEU^\dagger$ to get single-particle energies E_a (and E_α^0 for H_0). The impurity entropy as a function of temperature T is then given by

$$\mathcal{S}_{\text{imp}}(T) = \mathcal{S}(T) - \mathcal{S}_0(T), \quad (\text{C1a})$$

$$\mathcal{S}_{(0)}(T) = -\sum_\alpha f_\alpha^{(0)} \log f_\alpha^{(0)} + (1-f_\alpha^{(0)}) \log(1-f_\alpha^{(0)}), \quad (\text{C1b})$$

where $f_\alpha^{(0)} \equiv f_{\text{FD}}(E_\alpha^{(0)}; T)$ is the occupation of the single-particle eigenmodes. In order to negate even-odd oscillations, we also need to average over two z shifts ($z = \frac{1}{2}, 1$).

The impurity spectral function (in the discrete model) is evaluated at E_α , with proper broadening

$$[\mathbf{A}_{\text{disc}}^{T=0}(E_\alpha)]_{mm'} = \frac{U_{m\alpha}^* U_{m'\alpha}}{|E_\alpha| \log \Lambda}, \quad (\text{C2})$$

where the impurity indices m, m' on the l.h.s. take the values 1, 2, and on the r.h.s. select the corresponding rows/columns in H . The thermal impurity correlations are then evaluated according to the second row of Eq. (29), replacing the integral by a discrete sum over the (single-particle) energies

$$\langle d_{m'}^\dagger d_m \rangle_T = \int_{-\infty}^{\infty} \mathbf{A}_{mm'}^{T=0}(\omega) f_{\text{FD}}(\omega) d\omega \rightarrow \sum_\alpha \frac{U_{m'\alpha} U_{m\alpha}^*}{e^{E_\alpha/T} + 1}. \quad (\text{C3})$$

In the continuum limit, we already start from an expression for the impurity spectral function, i.e., Eq. (28), and then obtain the thermal correlations by numerically solving the integral in Eq. (29) [Eq. (C3) here].

[1] M. Z. Hasan and C. L. Kane, Colloquium: Topological insulators, *Rev. Mod. Phys.* **82**, 3045 (2010).
[2] X.-L. Qi and S.-C. Zhang, Topological insulators and superconductors, *Rev. Mod. Phys.* **83**, 1057 (2011).
[3] J. Kondo, Resistance Minimum in Dilute Magnetic Alloys, *Progress of Theoretical Physics* **32**, 37 (1964).

[4] A. C. Hewson, *The Kondo Problem to Heavy Fermions*, Cambridge Studies in Magnetism (Cambridge University Press, Cambridge, 1993).
[5] N. Andrei, K. Furuya, and J. H. Lowenstein, Solution of the Kondo problem, *Rev. Mod. Phys.* **55**, 331 (1983).
[6] A. Tselick and P. Wiegmann, Exact results in the theory

- of magnetic alloys, *Advances in Physics* **32**, 453 (1983).
- [7] I. Affleck, A current algebra approach to the Kondo effect, *Nuclear Physics B* **336**, 517 (1990).
- [8] I. Affleck and A. W. W. Ludwig, The Kondo effect, conformal field theory and fusion rules, *Nuclear Physics B* **352**, 849 (1991).
- [9] A. O. Gogolin, A. A. Nersisyan, and A. M. Tsvelik, *Bosonization and Strongly Correlated Systems* (Cambridge university press, 2004).
- [10] M. A. Ruderman and C. Kittel, Indirect Exchange Coupling of Nuclear Magnetic Moments by Conduction Electrons, *Phys. Rev.* **96**, 99 (1954).
- [11] T. Kasuya, A Theory of Metallic Ferro- and Antiferromagnetism on Zener's Model, *Progress of Theoretical Physics* **16**, 45 (1956).
- [12] K. Yosida, Magnetic Properties of Cu-Mn Alloys, *Phys. Rev.* **106**, 893 (1957).
- [13] S. Doniach, The Kondo lattice and weak antiferromagnetism, *Physica B+C* **91**, 231 (1977).
- [14] C. Jayaprakash, H. R. Krishna-murthy, and J. W. Wilkins, Two-Impurity Kondo Problem, *Phys. Rev. Lett.* **47**, 737 (1981).
- [15] B. A. Jones and C. M. Varma, Study of two magnetic impurities in a Fermi gas, *Phys. Rev. Lett.* **58**, 843 (1987).
- [16] B. A. Jones, C. M. Varma, and J. W. Wilkins, Low-Temperature Properties of the Two-Impurity Kondo Hamiltonian, *Phys. Rev. Lett.* **61**, 125 (1988).
- [17] R. M. Fye and J. E. Hirsch, Quantum Monte Carlo study of the two-impurity Kondo Hamiltonian, *Phys. Rev. B* **40**, 4780 (1989).
- [18] R. M. Fye, "Anomalous fixed point behavior" of two Kondo impurities: A reexamination, *Phys. Rev. Lett.* **72**, 916 (1994).
- [19] I. Affleck, A. W. W. Ludwig, and B. A. Jones, Conformal-field-theory approach to the two-impurity Kondo problem: Comparison with numerical renormalization-group results, *Phys. Rev. B* **52**, 9528 (1995).
- [20] J. Gan, Solution of the two-impurity Kondo model: Critical point, Fermi-liquid phase, and crossover, *Phys. Rev. B* **51**, 8287 (1995).
- [21] J. B. Silva, W. L. C. Lima, W. C. Oliveira, J. L. N. Mello, L. N. Oliveira, and J. W. Wilkins, Particle-Hole Asymmetry in the Two-Impurity Kondo Model, *Phys. Rev. Lett.* **76**, 275 (1996).
- [22] N. Andrei, G. T. Zimányi, and G. Schön, Quantum phase transition in coupled quantum dots, *Phys. Rev. B* **60**, R5125 (1999).
- [23] C. L. Kane and E. J. Mele, Quantum Spin Hall Effect in Graphene, *Phys. Rev. Lett.* **95**, 226801 (2005).
- [24] B. A. Bernevig, T. L. Hughes, and S.-C. Zhang, Quantum Spin Hall Effect and Topological Phase Transition in HgTe Quantum Wells, *Science* **314**, 1757 (2006).
- [25] J. Gao, W. Chen, X. C. Xie, and F.-c. Zhang, In-plane noncollinear exchange coupling mediated by helical edge states in quantum spin Hall systems, *Phys. Rev. B* **80**, 241302 (2009).
- [26] Y.-W. Lee and Y.-L. Lee, Electrical control and interaction effects of the RKKY interaction in helical liquids, *Phys. Rev. B* **91**, 214431 (2015).
- [27] V. D. Kurilovich, P. D. Kurilovich, and I. S. Burmistrov, Indirect exchange interaction between magnetic impurities near the helical edge, *Phys. Rev. B* **95**, 115430 (2017).
- [28] O. M. Yevtushenko and V. I. Yudson, Kondo Impurities Coupled to a Helical Luttinger Liquid: RKKY-Kondo Physics Revisited, *Phys. Rev. Lett.* **120**, 147201 (2018).
- [29] V. Cheianov and L. I. Glazman, Mesoscopic Fluctuations of Conductance of a Helical Edge Contaminated by Magnetic Impurities, *Phys. Rev. Lett.* **110**, 206803 (2013).
- [30] B. L. Altshuler, I. L. Aleiner, and V. I. Yudson, Localization at the Edge of a 2D Topological Insulator by Kondo Impurities with Random Anisotropies, *Phys. Rev. Lett.* **111**, 086401 (2013).
- [31] C.-H. Hsu, P. Stano, J. Klinovaja, and D. Loss, Nuclear-spin-induced localization of edge states in two-dimensional topological insulators, *Phys. Rev. B* **96**, 081405 (2017).
- [32] B. I. Halperin, Quantized Hall conductance, current-carrying edge states, and the existence of extended states in a two-dimensional disordered potential, *Phys. Rev. B* **25**, 2185 (1982).
- [33] A. M. Tsvelick, The thermodynamics of multichannel Kondo problem, *J. Phys. C: Solid State Phys.* **18**, 159 (1985).
- [34] A. Yu. Kitaev, Fault-tolerant quantum computation by anyons, *Annals of Physics* **303**, 2 (2003).
- [35] C. Nayak, S. H. Simon, A. Stern, M. Freedman, and S. Das Sarma, Non-Abelian anyons and topological quantum computation, *Rev. Mod. Phys.* **80**, 1083 (2008).
- [36] Y. Komijani, Isolating Kondo anyons for topological quantum computation, *Phys. Rev. B* **101**, 235131 (2020).
- [37] P. L. S. Lopes, I. Affleck, and E. Sela, Anyons in multichannel Kondo systems, *Phys. Rev. B* **101**, 085141 (2020).
- [38] D. Gabay, C. Han, P. L. S. Lopes, I. Affleck, and E. Sela, Multi-impurity chiral Kondo model: Correlation functions and anyon fusion rules, *Phys. Rev. B* **105**, 035151 (2022).
- [39] M. Lotem, E. Sela, and M. Goldstein, Manipulating Non-Abelian Anyons in a Chiral Multichannel Kondo Model, *Phys. Rev. Lett.* **129**, 227703 (2022).
- [40] Z. Iftikhar, S. Jezouin, A. Anthore, U. Gennser, F. D. Parmentier, A. Cavanna, and F. Pierre, Two-channel Kondo effect and renormalization flow with macroscopic quantum charge states, *Nature* **526**, 233 (2015).
- [41] Z. Iftikhar, A. Anthore, A. K. Mitchell, F. D. Parmentier, U. Gennser, A. Ouerghi, A. Cavanna, C. Mora, P. Simon, and F. Pierre, Tunable quantum criticality and superballistic transport in a "charge" Kondo circuit, *Science* **360**, 1315 (2018).
- [42] L. A. Landau, E. Cornfeld, and E. Sela, Charge Fractionalization in the Two-Channel Kondo Effect, *Phys. Rev. Lett.* **120**, 186801 (2018).
- [43] G. A. R. van Dalum, A. K. Mitchell, and L. Fritz, Wiedemann-Franz law in a non-Fermi liquid and Majorana central charge: Thermoelectric transport in a two-channel Kondo system, *Phys. Rev. B* **102**, 041111 (2020).
- [44] T. K. T. Nguyen and M. N. Kiselev, Thermoelectric Transport in a Three-Channel Charge Kondo Circuit, *Phys. Rev. Lett.* **125**, 026801 (2020).
- [45] C. Han, Z. Iftikhar, Y. Kleeorin, A. Anthore, F. Pierre, Y. Meir, A. K. Mitchell, and E. Sela, Fractional Entropy of Multichannel Kondo Systems from Conductance-Charge Relations, *Phys. Rev. Lett.* **128**, 146803 (2022).
- [46] W. Pouse, L. Peeters, C. L. Hsueh, U. Gennser, A. Cavanna, M. A. Kastner, A. K. Mitchell, and D. Goldhaber-Gordon, Quantum simulation of an exotic quantum critical point in a two-site charge Kondo circuit, *Nat. Phys.* **1** (2023).

- [47] K. G. Wilson, The renormalization group: Critical phenomena and the Kondo problem, *Rev. Mod. Phys.* **47**, 773 (1975).
- [48] R. Bulla, T. A. Costi, and T. Pruschke, Numerical renormalization group method for quantum impurity systems, *Rev. Mod. Phys.* **80**, 395 (2008).
- [49] K. Ingersent, B. A. Jones, and J. W. Wilkins, Study of the two-impurity, two-channel Kondo Hamiltonian, *Phys. Rev. Lett.* **69**, 2594 (1992).
- [50] V. L. Campo and L. N. Oliveira, Alternative discretization in the numerical renormalization-group method, *Phys. Rev. B* **72**, 104432 (2005).
- [51] A. K. Mitchell, E. Sela, and D. E. Logan, Two-Channel Kondo Physics in Two-Impurity Kondo Models, *Phys. Rev. Lett.* **108**, 086405 (2012).
- [52] A. K. Mitchell, P. G. Derry, and D. E. Logan, Multiple magnetic impurities on surfaces: Scattering and quasi-particle interference, *Phys. Rev. B* **91**, 235127 (2015).
- [53] B. Lechtenberg, F. Eickhoff, and F. B. Anders, Realistic quantum critical point in one-dimensional two-impurity models, *Phys. Rev. B* **96**, 041109 (2017).
- [54] F. Eickhoff, B. Lechtenberg, and F. B. Anders, Effective low-energy description of the two-impurity Anderson model: RKKY interaction and quantum criticality, *Phys. Rev. B* **98**, 115103 (2018).
- [55] F. Eickhoff and F. B. Anders, Strongly correlated multi-impurity models: The crossover from a single-impurity problem to lattice models, *Phys. Rev. B* **102**, 205132 (2020).
- [56] J.-G. Liu, D. Wang, and Q.-H. Wang, Quantum impurities in channel mixing baths, *Phys. Rev. B* **93**, 035102 (2016).
- [57] B. Bruognolo, N.-O. Linden, F. Schwarz, S.-S. B. Lee, K. Stadler, A. Weichselbaum, M. Vojta, F. B. Anders, and J. von Delft, Open Wilson chains for quantum impurity models: Keeping track of all bath modes, *Phys. Rev. B* **95**, 121115 (2017).
- [58] R. Žitko, Adaptive logarithmic discretization for numerical renormalization group methods, *Computer Physics Communications* **180**, 1271 (2009).
- [59] R. Žitko and T. Pruschke, Energy resolution and discretization artifacts in the numerical renormalization group, *Phys. Rev. B* **79**, 085106 (2009).
- [60] A. Weichselbaum, Tensor networks and the numerical renormalization group, *Phys. Rev. B* **86**, 245124 (2012).
- [61] A. K. Mitchell, M. R. Galpin, S. Wilson-Fletcher, D. E. Logan, and R. Bulla, Generalized Wilson chain for solving multichannel quantum impurity problems, *Phys. Rev. B* **89**, 121105 (2014).
- [62] K. M. Stadler, A. K. Mitchell, J. von Delft, and A. Weichselbaum, Interleaved numerical renormalization group as an efficient multiband impurity solver, *Phys. Rev. B* **93**, 235101 (2016).
- [63] A. Weichselbaum, Non-abelian symmetries in tensor networks: A quantum symmetry space approach, *Annals of Physics* **327**, 2972 (2012).
- [64] A. Weichselbaum, X-symbols for non-Abelian symmetries in tensor networks, *Phys. Rev. Research* **2**, 023385 (2020).
- [65] J. R. Schrieffer and P. A. Wolff, Relation between the Anderson and Kondo Hamiltonians, *Phys. Rev.* **149**, 491 (1966).
- [66] R. Horodecki, P. Horodecki, M. Horodecki, and K. Horodecki, Quantum entanglement, *Rev. Mod. Phys.* **81**, 865 (2009).
- [67] A. Kamenev, *Field Theory of Non-Equilibrium Systems* (Cambridge University Press, Cambridge, 2011).
- [68] P. A.-C. Ferrer, O. M. Yevtushenko, and A. Weichselbaum, RKKY to Kondo crossover in Helical Edge of a Topological Insulator (2022), [arxiv:arXiv:2208.02275](https://arxiv.org/abs/2208.02275).
- [69] S.-S. B. Lee and A. Weichselbaum, Adaptive broadening to improve spectral resolution in the numerical renormalization group, *Phys. Rev. B* **94**, 235127 (2016).
- [70] J. J. Sakurai and J. Napolitano, *Modern Quantum Mechanics*, 2nd ed. (Cambridge University Press, Cambridge, 2017).